AUTONOMOUS SPACE PROCESSOR FOR ORBITAL DEBRIS

Summary Report
(1990 - 91)

Submitted By:
Dr. Kumar Ramohalli
Micky Marine
James Colvin
Richard Crockett
Lee Sword
Jennifer Putz
Sheri Woelfle

University of Arizona
Tucson,Arizona

Submitted:
Universities Space Research Association
7th Annual Summer Conference
NASA/Kennedy Space Center
JUNE 17-21, 1991

AUTONOMOUS SPACE PROCESSOR FOR ORBITAL DEBRIS

Summary Report

(1990 - 91)

Submitted By:
Dr. Kumar Ramohalli
Micky Marine
James Colvin
Richard Crockett
Lee Sword
Jennifer Putz
Sheri Woelfle

University of Arizona
Tucson,Arizona

Submitted:
Universities Space Research Association
7th Annual Summer Conference
NASA/Kennedy Space Center
JUNE 17-21, 1991

ADVANCED DESIGN FOR ORBITAL DEBRIS REMOVAL IN SUPPORT OF SOLAR SYSTEM EXPLORATION

Dr. Kumar Ramohalli
and
Micky Marine, James Colvin, Richard Crockett,
Lee Sword, Jennifer Putz, Sheri Woelfle
University of Arizona
Aerospace and Mechanical Engineering Department
Tucson, Arizona 85721

Abstract

This is a brief description of the USRA-sponsored design project at the University of Arizona. The development of an Autonomous Space Processor for Orbital Debris (ASPOD) is the ultimate goal of this project. The nature of this craft, which will process, in-situ, orbital debris utilizing resources available in low Earth orbit (LEO) is explained. the serious problem of orbital debris is briefly described and the nature of the large debris population is outlined. This years focus was on the development of a versatile robotic manipulator to augment an existing robotic arm, the incorporation of remote operation of the robotic arms and the formulation of optimal (time and energy) trajectory planning algorithms for coordinated robotic arms. The mechanical design of the new arm is described in detail. The versatile work envelope is explained showing the flexibility of the new design. Several telemetry-communication systems are described which will enable the remote operation of the robotic arms. The trajectory planning algorithms are fully developed for both the time optimal and energy optimal problems. The time optimal problem is solved using phase plane techniques while the energy optimal problem is solved using dynamic programming.

Introduction

The problems presented by orbital debris have been gaining attention in recent years. Science writers [1–4] and the popular news media [5–9] have lucidly described these problems. The orbital debris problem merited a report from the General Accounting Office [10] describing the threats imposed on the future space station and other space operations. The Advanced Design team at the University of Arizona continues to develop a spacecraft which will economically remove the larger debris through local resource utilization. The fundamental idea is to concentrate solar energy into a point focus, cut the debris into precise shapes that the robotic arms can assemble into a manageable configuration. After having processed several debris pieces three disposal modes exist - 1.) retrieval by the Shuttle, 2.) precise splashdown into the oceans, or 3.) planned burnup during atmospheric reentry.

A study conducted by the University of Arizona in 1989 showed that there were 386 objects in Earth orbit that qualify as large debris (having a mass greater than 1500 kilograms). Each of the objects included in this list have sufficient orbital lifetimes that will ensure their existence past the year 2000. This study also identified several specific inclinations in which a majority of the large debris exists (fig. 1).

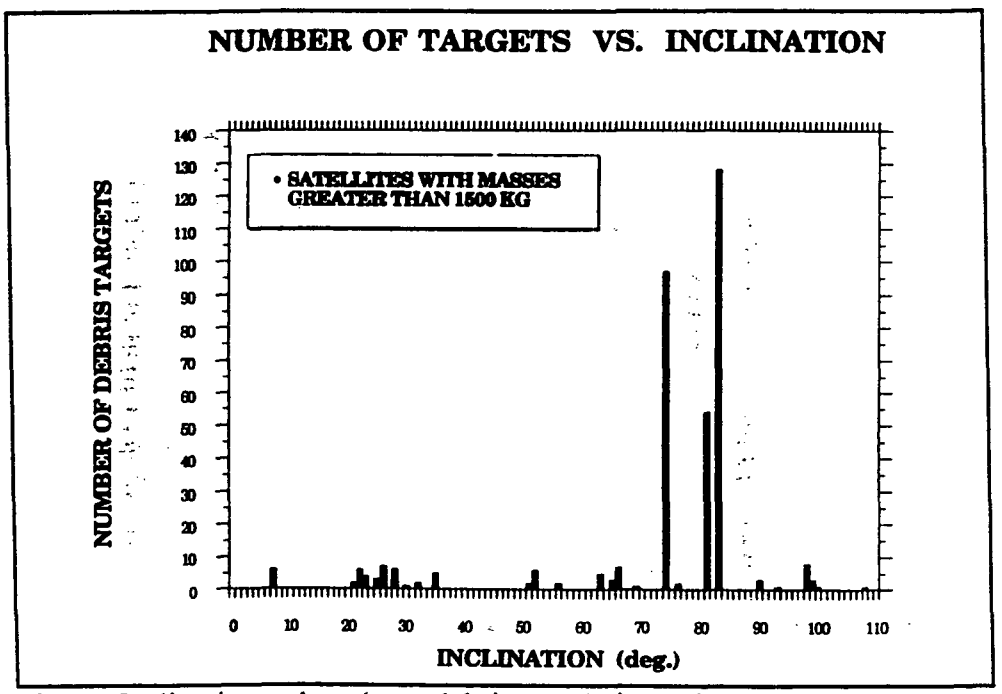

Fig. 1. Inclinations where large debris population exists.

Mission feasibility studies have shown that one of the envisioned spacecraft can process at least five of the large pieces of debris with reasonable propellant requirements [11]. This is accomplished by taking advantage of nodal regression differences and through the use of the classic Hohmann transfer.

This years work focused on the development of a versatile robotic manipulator, investigation of remote operation of the existing solar collector and new robotic arms, and the formulation of trajectory planning algorithms for coordinated robotic arms carrying a common object. This report is a summary of the work and explains the details involved.

Consistent with the USRA philosophy, new undergraduate students were brought on board. This year, five new students were involved in the Autonomous Space Processor for Orbital Debris (ASPOD) design. Four new students were involved with the design and fabrication of a robotic manipulator, while the other new student refined the solar tracking device and investigated telemetry systems for future use. In addition, two local high school students were actively involved in the project.

The support from USRA and technical monitoring of Mr. James D. Burke of JPL are gratefully acknowledged. Mr. Milton Schick contributed towards the new robotic arm.

ROBOT MANIPULATOR ARM

Design requirements for the robot manipulator arm call for a rather large working envelope. The arm must be able to retrieve, at a safe distance, the target debris, it must manipulate the debris at the focal point, position cut pieces near the mirrors, and stow unusable pieces in the storage bin.For the one-fifth scale prototype a stationary robot would need a reach of over ten feet. This years design team developed a six degree of freedom robotic arm with the additional feature of a mobile mount that reduced the necessary lengths of each segment. Upon assembly and testing, the robotic arm satisfied all design specifications.

DESIGN OF THE MOBILE MOUNT

The mobile mount is a rotating base for a manipulator. The base, or arm, is designed to maximize the working envelope of the manipulator while minimizing its length and weight requirements.

A top view of the mount is shown in figure 1. The power needed for the mobile mount comes from a parallel shaft TENV gearmotor, which is geared down before driving the shaft that goes through the ASPOD platform. The shaft is supported by ball bearings and drives an arm which sits on shoulders machined into the shaft. The other end of the arm rotates with the shaft, thus the mobility. The manipulator will "ride" on the far end of the arm near the guide wheel assembly. The guide wheel assembly prevents the arm from moving normal to the ASPOD platform as well as resisting torsional twisting. The arm is guided by a track that is attached to the ASPOD platform.

SHAFT ASSEMBLY

The center point of the mobile mount assembly is the central shaft. This shaft supports the torque generated by the weight of the manipulator. The maximum torque, as defined by the static and dynamic model of the manipulator, is approximated at 55 lbf ft. The material chosen for the shaft is carbon steel because of its relatively high modules of rigidity and availability. The diameter

Fig. #1

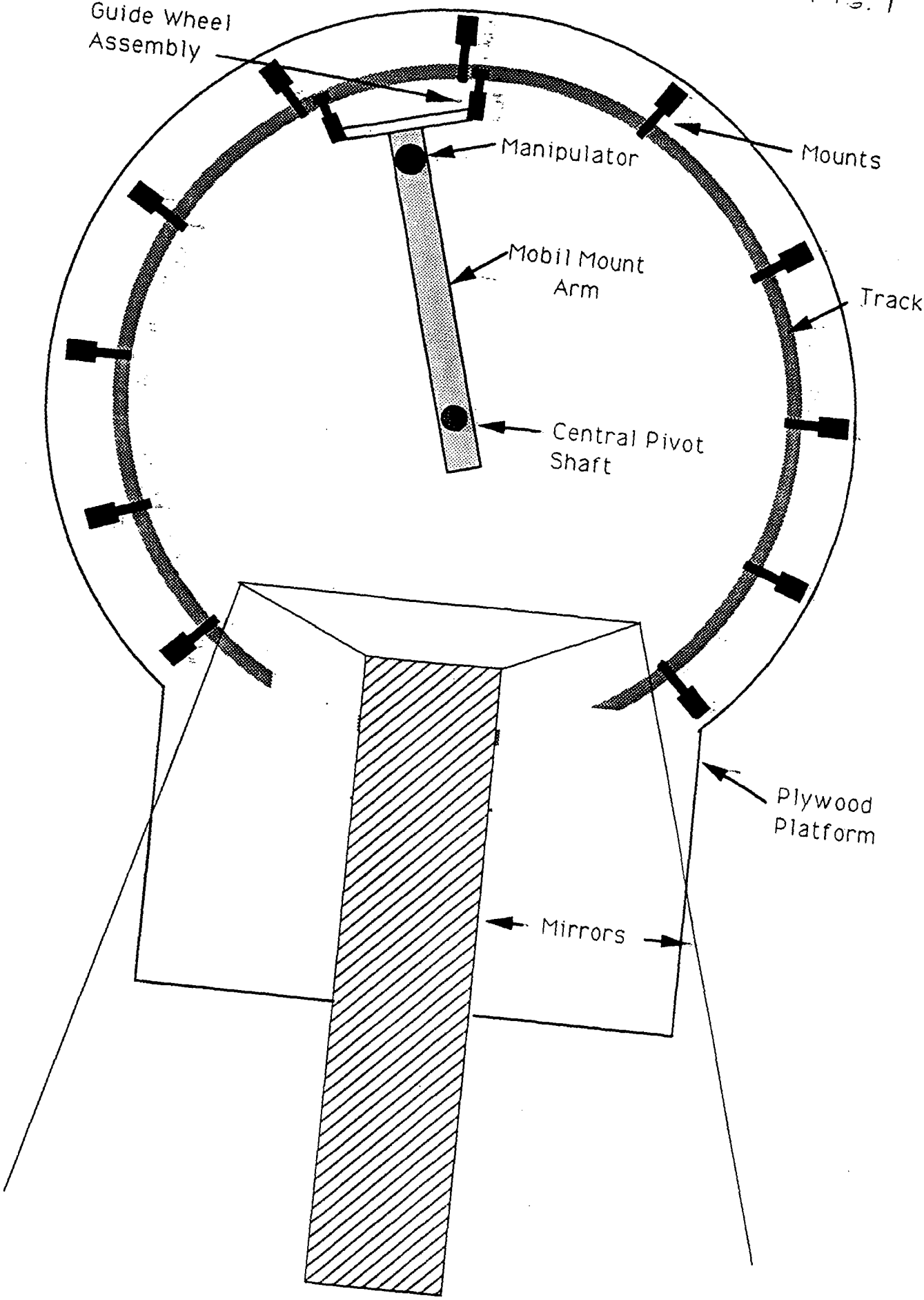
Guide Wheel Assembly
Manipulator
Mounts
Mobil Mount Arm
Track
Central Pivot Shaft
Plywood Platform
Mirrors

CENTRAL SHAFT ASSEMBLY (FIG. #2)

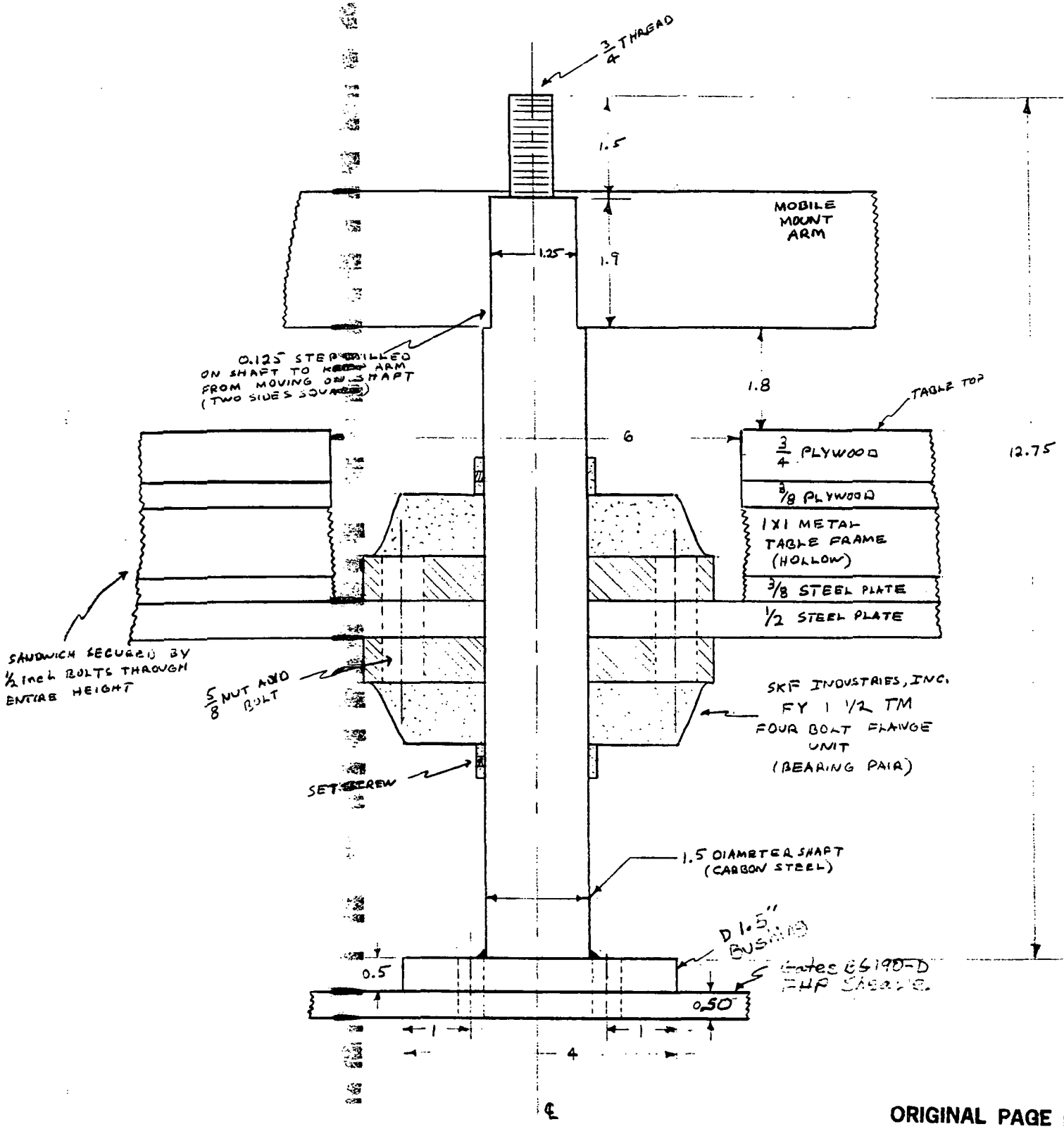

ORIGINAL PAGE IS OF POOR QUALITY

SCALE 1" = 2"

(all dimensions in inches)

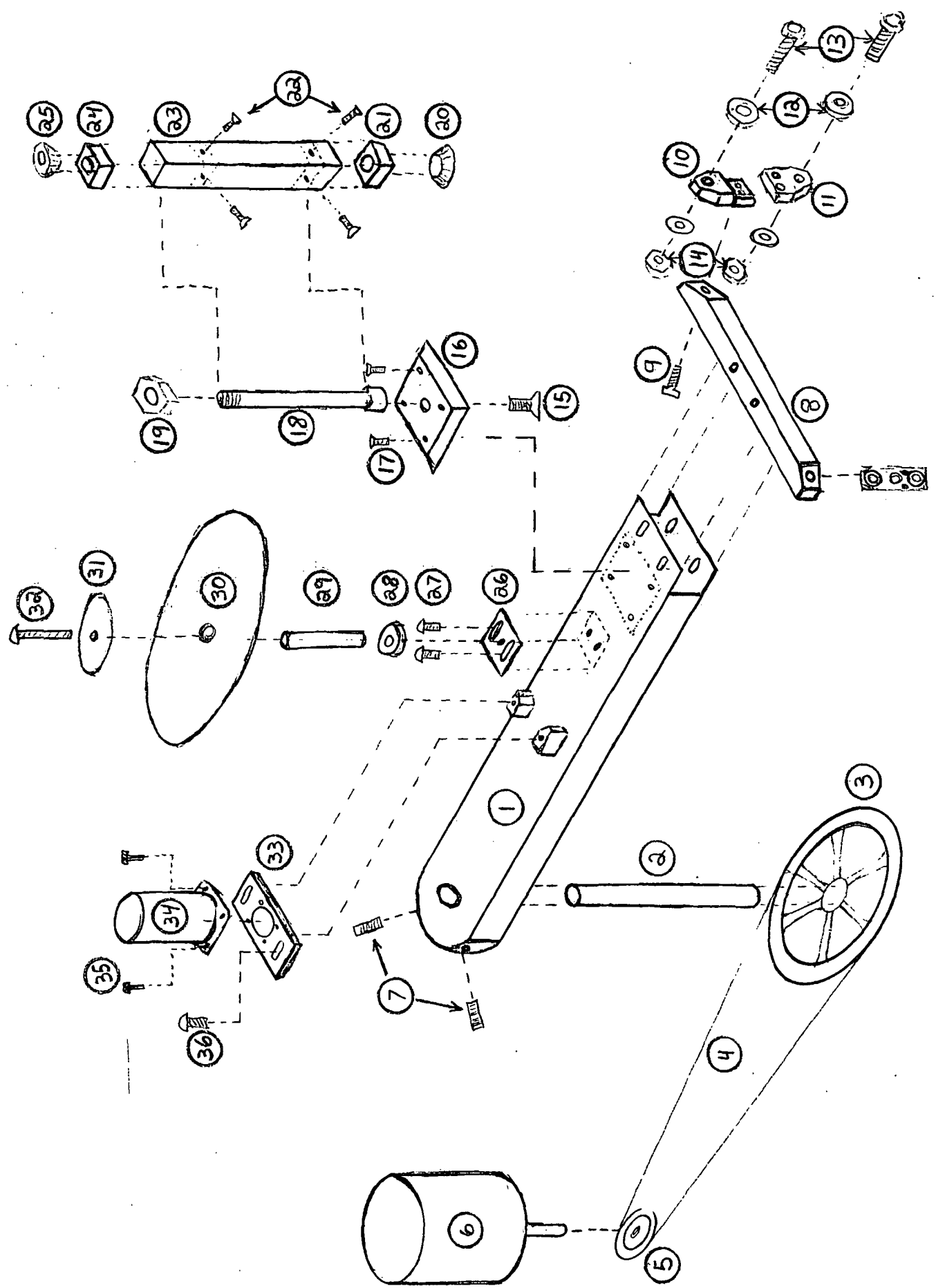

ORIGINAL PAGE
COLOR PHOTOGRAPH

Key to Figure 3

ID#	PART	SPECIFICATIONS	#
1	MOBILE ARM	2" X 5" X 32" 1/16" THICK	1
2	CENTRAL PIN	1.5" 22" COLD ROLLED STEEL	1
3	MAIN SHEAVE	GATES LIGHT DUTY SHEAVE 18.4"	1
4	DRIVE BELT	GATES HIGH-POWER DUBL-V 84"	1
5	SECONDARY SHEAVE	GATES LIGHT DUTY SHEAVE 2.84"	1
6	DRIVE MOTOR	DAYTON PARALLEL SHAFT TENV	1
7	SET SCREW	1/4-20 X 1"	2
8	WHEEL GUIDE SUPPORT	1.5 X 1.5 X 11" 6061-T6	1
9	MOUNTING BOLT	1/4-20 X 2" ALLEN CAP BOLT	2
10	UPPER WHEEL GUIDE	2.5 X 1.5 X 1.5 6061-T6	2
11	LOWER WHEEL GUIDE	1.5 X 1.5 X 1.5 6061-T6	2
12	GUIDE WHEEL	6200 SERIES DOUBLE SHIELDED	4
13	GUIDE WHEEL SHAFT	10 X 40 mm GRADE 8 BOLT	4
15	SHAFT BOLT	1/2-20 X 1" FLAT HEAD BOLT	1
16	SUPPORT PLATE	5" X 5" X 3/4" 6061-T6	1
18	BEARING SHAFT	3/4 > 11/16 COLD ROLLED STEEL	1
19	SHAFT NUT	5/8 X 20	1
20	LOWER TAPER BEARING	.545 X 1.57 X .68" NTN	1
21	LOWER BEARING BLOCK	1.75 X 1.75 X 1.5 6061-T6	1
23	LINK # 1	2 X 2 X 12 X 1/16" THICK	1
24	UPPER BEARING BLOCK	1.75 X 1.75 X 1.5 6061-T6	1
25	UPPER TAPER BEARING	.545 X 1.57 X .68" NTN	1
26	SUPPORT PLATE	2 X 2 X .5 6061-T6	1
27	MOUNTING SCREWS	10-24 X 3/4" MACHINE SCREW	2
28	IDLER BEARING	1/4 ID DOUBLE SHIELDED	2
29	IDLER SHAFT	3/16 X 1.2" STAINLESS STEEL	1
30	LARGE IDLER SPROCKET	Flex-E-Gear 6.0 P.D.	1
31	SMALL IDLER SPROCKET	Flex-E-Gear 0.83 P.D.	1
32	SUPPORT BOLT	10/32 X 3/4" MACHINE SCREW	2
33	MOTOR MOUNT	1/4 X 1.5 X 4" 6061-T6	1
34	DRIVE MOTOR	GLOBE 12 V DC GEARMOTOR	1

chosen for this design was 1.5 inch. A 13.5 X 14.5 X 0.5 steel plate supports the shaft. This material was chosen for its high strength and availability. The plate was mounted beneath the ASPOD platform, secured by half inch bolts to the metal frame of the platform. SKF Industries, Inc. bearings number FY 1 1/2 TM bearings were used to support the shaft. THese bearings support both radial and axial loads and are relatively low in cost. The bearings make a sandwich around the steel plate thus supporting the shaft (see Figure 2).

MOBILE ARM and WHEEL GUIDE ASSEMBLY

This discussion will focus on the design, fabrication, and testing of the mobile arm and wheel guide assembly to be used on the ASPOD prototype platform. The primary considerations in the design of the mobile arm were: (1) attachment to the central shaft, (2) torsional deflection under the maximum calculated load, and (3) attachment to the wheel guide assembly. A 1.5 inch central shaft extends from the top of the platform, the maximum torque on the arm was calculated at 650 lb/in. The wheel guide assembly will be mounted to 6061-T6 1.5 inch square stock. With these considerations in mind, the arm was designed and fabricated out of 2 X 5 inch rectangular aluminum (wall thickness = 3/16 inch) which was determined to satisfy the design requirements. The dimensions and machining modifications are shown in Figure 3. The wheel guide assembly is responsible for supporting the mobile arm vertically as well as resisting torsional twisting. It was determined that four 6200 series double shielded ball bearings will be supported by 10 X 40 mm grade 8 bolts mounted in adjustable supports machined from 6061-T6 aluminum stock. Dimensions and hardware are shown in Figure 3. After assembly, testing indicated that all components performed as designed. There was no measurable deflection at the wheel/track interface or at the shaft/arm interface.

TRACK and TRACK MOUNTS

For the mobile arm, a track was required to allow for movement from one side of the ASPOD platform to the other. The track needed

FIG. #5

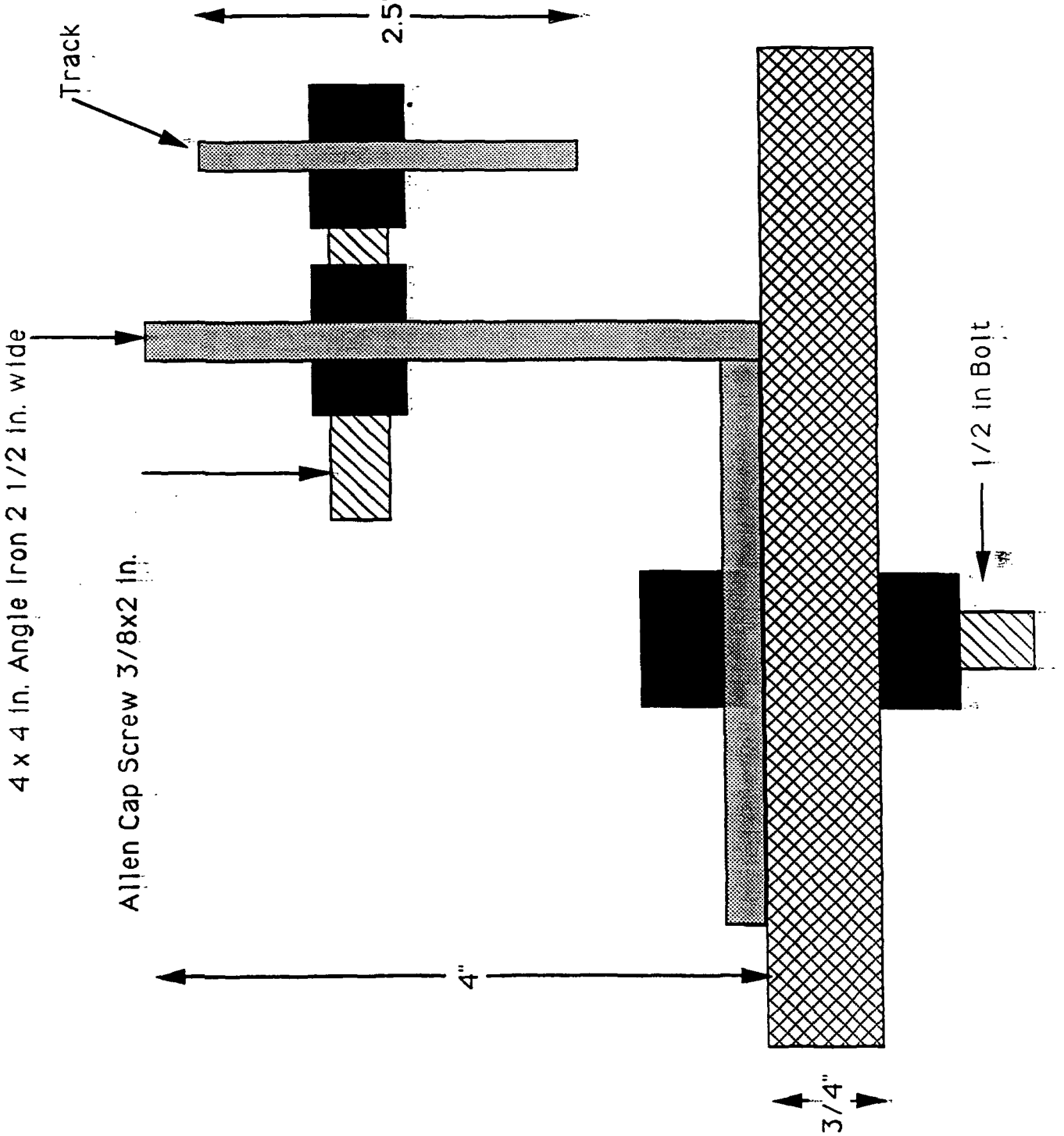
Track
2.5"
4 x 4 in. Angle Iron 2 1/2 in. wide
Allen Cap Screw 3/8x2 in.
1/2 in Bolt
4"
3/4"

to allow for a guide wheel assembly that would resist motion perpendicular to the mobile mount. After much consideration we decided to use a piece of 3/16 inch cold rolled steel 2 1/2 inches wide. The piece of steel, approximately 12 ft long, was formed into a 5 ft diameter circle. The track was then mounted to a piece of 3/4 inch plywood which was mounted to the ASPOD platform (see Figure 1). To mount the track to the ASPOD platform, mounts that would allow for complete motion of the mobile arm on the inner diameter of the track were required. To do this, 3/8 inch holes were drilled every 6 inches in the track. A 3/8 X 2 allen cap screw was used to mount the track to a 4 X 4 inch piece of angle that was mounted to the plywood platform (see Figure 5). This mounting system allowed for the mobile arm guide wheel assembly to mount as shown in Figure 5, which allows for the complete motion of the mobile arm in the inner diameter of the track and would also have no motion perpendicular to the mobile mount.

MANIPULATOR LINK AND JOINT MATERIAL

After the consideration of various materials, the final decision was made to use the Aluminum alloy 6061-T6 for the construction of the manipulator links and joints. This alloy, which contains both magnesium and silicon, was chosen because of its good formability, machinability, weldability, and its good corrosion resistance properties. The temper designation, T6, means this alloy has been solution treated and artificially aged. The major reason for its selection is its relative ease of availability and its relative low cost compared to the other materials which were considered. Table 1 lists some of the important physical and mechanical properties.

PROPERTIES	UNITS	VALUE
Yield Strength	kpsi	40
Ultimate Strength	kpsi	45
Modulus of Elasticity	10^6 psi	10.3
Modulus of Rigidity	10^6 psi	3.8
Density	lbs/in^3	0.098
Strength to Weight Ratio	10^6 in	105.1

Table 1. Al 6061-T6 Properties

DEFLECTION AND MOMENT ANALYSIS

The manipulator links will be numbered I, II, and III, beginning at the mobile mount and moving towards the free end of the arm. The shape and dimensions of each link were chosen by using a combination of the availability of a particular material shape and the minimum size needed to attach the necessary actuators to the link's end. Table 2 shows the dimensions of the links. All links are hollow square tubes enabling the routing of wires through their centers.

LINK	DIMENSION (in)	WEIGHT (lb)
I (square)	2 x 2 x 1/8 x 12	1.1
II (square)	2 x 2 x 1/8 x 24	2.2
III (square)	2 x 2 x 1/8 x 12	1.1

Table 2. Link Dimensions

Using these dimensions, a deflection analysis was performed to make certain that these links would meet the minimum deflection specification of a maximum deflection of 1 cm (0.39 in). This is defined as the difference in deflection between the loaded link and the unloaded link. It will be assumed that the unloaded link will have a 100% repeatability in positioning. Then, if the loaded link can be positioned within 0.39 in. of the unloaded link, the specification will be considered satisfied. A rough schematic of the assembled manipulator can be seen in figure 6. The dimensions shown are those dimensions which are necessary for a deflection and torque analysis. The deflection analysis can be seen in APPENDIX A and the results are listed in Table 3.

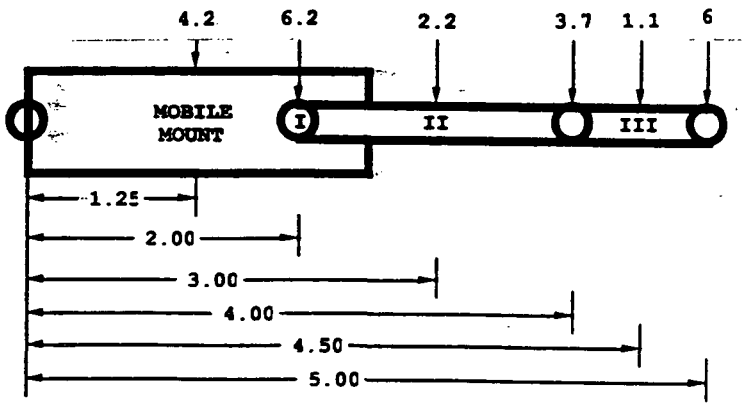

(weights in pounds)
(lengths in inches)

Figure 6. Deflection and Torque Parameters

LINK	Unloaded (in)	Loaded (in)	Difference (in)
III	0.0006	0.0007	0.0001
II	0.0134	0.0135	0.0001
I	0.0054	0.0054	< 0.0001

Table 3. Link Deflections

As is evident from the difference values seen in Table 3, the chosen link dimensions fully meet the deflection design specifications. Using these links, the moments developed at the attached end of each link were next calculated. These calculations can be found also in APPENDIX A and the loaded and unloaded values can be seen in Table 4.

LINK	UNLOADED	LOADED	DIFFERENCE
III	78.60 lb in	79.35 lb in	0.75 lb in
II	285.61 lb in	287.11 lb in	1.50 lb in
I	285.61 lb in	287.11 lb in	1.50 lb in
MOBILE MOUNT	888.0 lb in	891.75 lb in	3.75 lb in

Table 4. Link End Moment Requirement

These values are important as they can be translated into torque requirements for the actuators between the links if one considers static conditions only. It is obvious that any final torque values must contain dynamic as well as static requirements. The equation for the Lagrangian method (Equation 1) for determining torque clearly shows that the torque is

$$\tau = (ml_c^2 + I)\ddot{\theta} + mgl_c \cos\theta \qquad (1)$$

the sum of the potential energy (static) and kinetic energy (dynamic) terms. The necessary torques can be calculated from this equation ignoring the kinetic energy term if the angular acceleration can be kept several orders of magnitude less than the potential energy acceleration term "g". This will result in a situation where only static conditions will be necessary to

calculate torques. By investigating Figure 7, it is clear that if the time frame can be kept below 30 seconds, torque values can be established by considering static requirements alone, as the angular acceleration term will result in a dynamic value several orders of magnitude less than the static term.

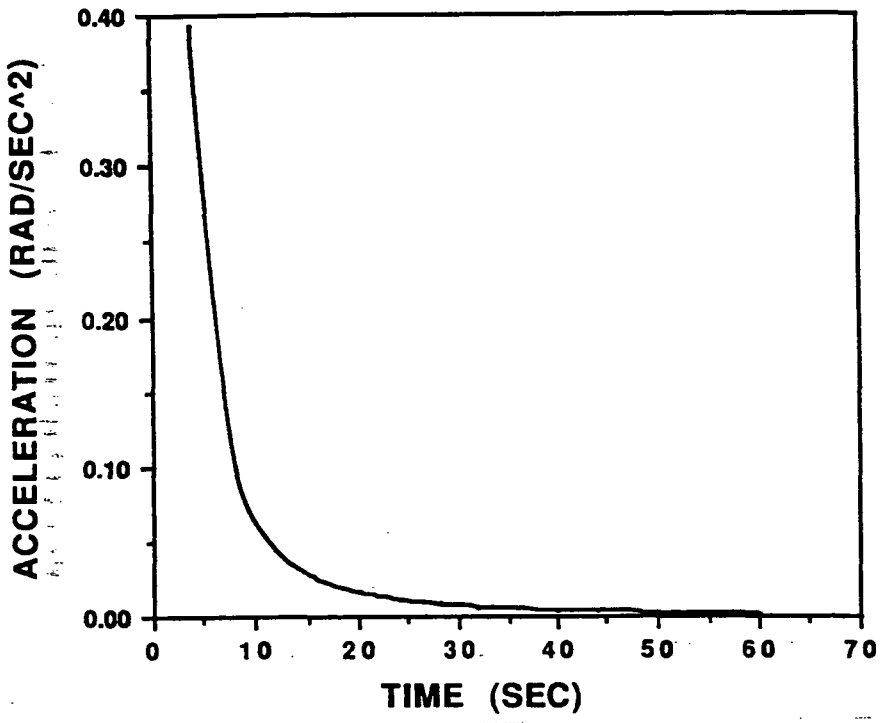

Figure 7 Acceleration Requirements

The time in this figure will be the time required to move the link from a vertically down position to a vertically up position. An angular velocity of 1/2 RPM corresponds to a time of 30 seconds, and it is clear that this time frame is approximately the point where the acceleration begins to rise very rapidly. The development of this figure can be found in APPENDIX B. It is clear that if the angular velocity can be kept at 1/2 RPM or lower, the Lagrangian equation can be solved to a high degree of accuracy while considering only the static or potential energy term alone. The Lagrangian equation shows clearly the difficulty in presenting on earth a manipulator designed for space. On earth, the

predominate acceleration term is gravity. As was previously shown, this is at least four times the magnitude of the angular acceleration term. However, in orbit this gravity term will be zero. Here, the angular acceleration will be the controlling parameter regardless of how small it might be.

JOINTS AND ACTUATORS

To join the manipulator links together, it was necessary to manufacture joints that allow the required degrees of freedom for each link. The joints are fashioned similar to a yoke, as shown in Figure 8 (# 42 an 53). The joints are made out of 6061-T6 Aluminum. The shaft is connected to the female portion of the yoke by anti-friction radial bearings, which also is connected to the male portion of the yoke as shown in Figure 8. For the rotary motion, a sprocket set is used in conjunction with a DC motor. For the motion between links I and II a double sprocket pair is used. For the motion between links II and III a single sprocket pair is used. The motors are connected to the links by means of a mount, also shown in Figure 8.

The torque required for the joint connecting links I and II is 4569.6 oz-in and 1257.6 oz-in for the joint connecting links II and III. The torques were calculated as described in the manipulator link section of this paper. For links I and II a double sprocket pair with a reduction of 16:1 was used. This resulted in the required torque at the motor to be 285.6 oz-in. A permanent magnet DC head motor with a maximum torque of 400 oz-in was used, this giving a safety factor of 1.4 at maximum load. For links II and III a single sprocket pair with a reduction of 6:1 was used. This resulted in the required torque at the motor to be 209.6 oz-in. For this, a permanent magnet DC gear head motor with a maximum torque of 400 oz-in was also used. This resulted in a safety factor of 1.9 at maximum load.

WRIST AND GRIPPER

The wrist assembly is designed to provide bending and rotational motion for the gripper. Bending motion is provided by

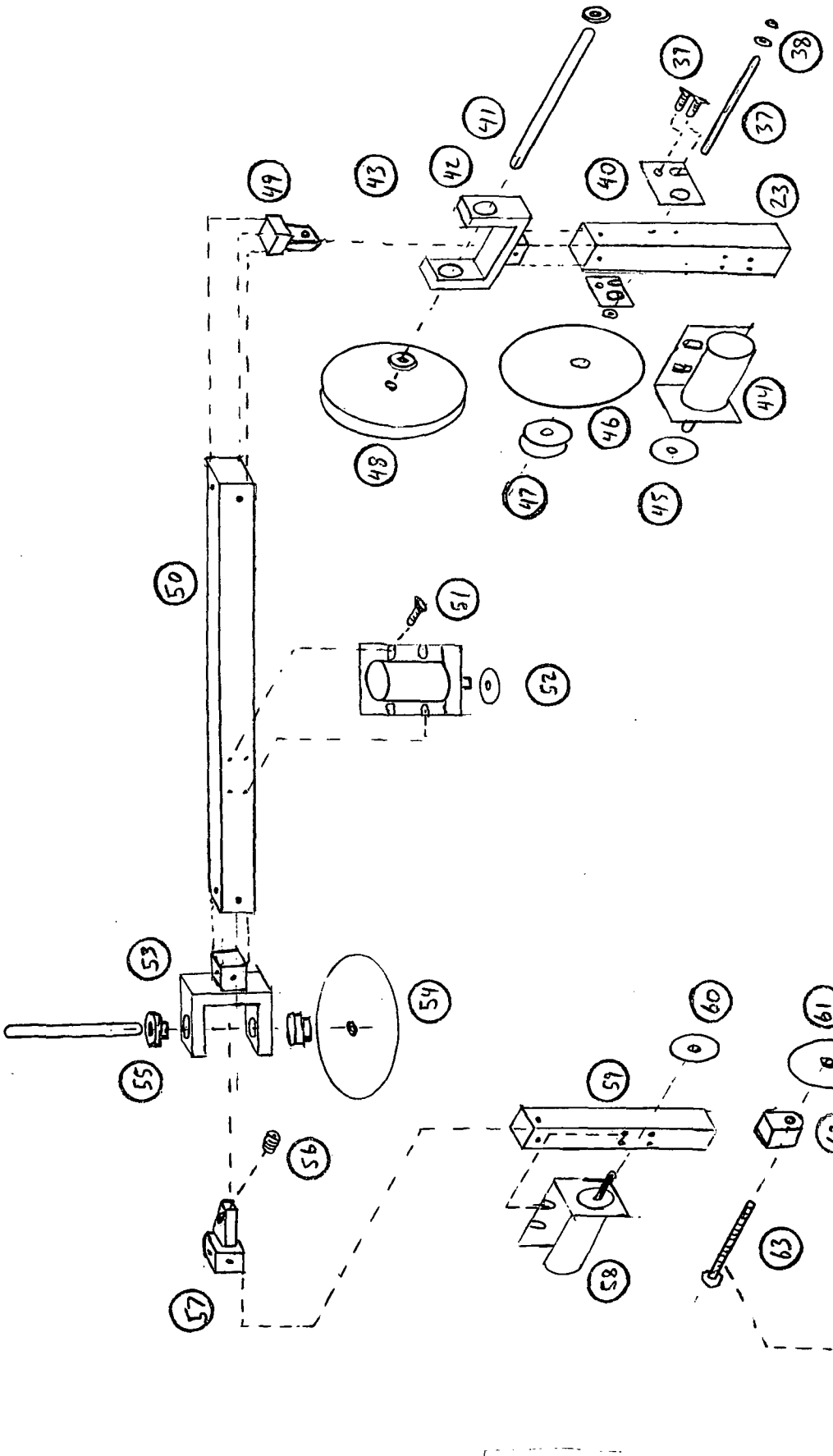

KEY TO FIGURE 8

ID #	PART	SPECIFICATIONS	#
23	LINK I	2 X 2 X 12 X 1/8" THICK	1
37	SHAFT	1/4" COLD ROLLED STEEL	1
38	BEARING	1/4" RADIAL	2
39	SCREWS	1/4-20 MACHINE SCREW	4
40	MOUNTING PLATE	2 1/4 X 1 1/2 X 1/4"	2
41	SHAFT	1/2" COLD ROLLED STEEL	1
42	YOKE (FEMALE)	Al 6061-T6	1
43	BEARING	1/2" ANTI-FRICTION (RADIAL)	2
44	MOTOR	DC PM (400 oz in)	1
45	SPROCKET	FLEX-E-GEAR 1.5 PD	1
46	SPROCKET	FLEX-E-GEAR 6.0 PD	1
47	SPROCKET PAIR	FLEX-E-GEAR 1.5 PD	2
48	SPROCKET PAIR	FLEX-E-GEAR 6.0 PD	2
49	YOKE (MALE)	Al 6061-T6	1
50	LINK II	2 X 2 X 21 X 1/8" THICK	1
51	SCREW	10-32 1/2" MACHINE SCREW	4
52	SPROCKET	FLEX-E-GEAR 1.0 PD	1
53	YOKE (FEMALE)	Al 6061-T6	1
55	BEARING	1/2" ANTI-FRICTION (RADIAL)	2
56	SET SCREW	5/16" X 3/4"	1
57	YOKE (MALE)	Al 6061-T6	1
58	MOTOR	DC PM (200 oz in)	1
59	LINK III	2 X 2 X 12 X 1/8" THICK	1
60	SPROCKET	FLEX-E-GEAR 1.0 PD	1
61	SPROCKET	FLEX-E-GEAR 3.0 PD	1
62	GRIPPER END BLOCK	Al 6061-T6	1
63	BOLT	1/2" X 4 1/2"	1

the rotation of a 200 oz-in DC gear head motor. As shown in Figure 8, a shaft connected to the gripper controls its rotational motion. This shaft is supported by two ball bearings positioned in a gripper end block machined from solid aluminium. The shaft is driven by a three to one ratio sprocket pair connected to the motor. A 3.5 inch extension piece connects the shaft to the supporting collar. This moves the rotation point closer to the center of gravity so the demands on the motor are reduced. With the extension piece and sprocket pair, there is a safety factor of 4.7 on this motor.

Rotational motion is provided by a DC motor connected directly to the gripper. The output shaft of the motor rotates a one quarter inch shaft which extends through a supporting collar. The supporting collar is a hollow aluminium piece which encases two ball bearings with a one quarter inch inner diameter. This shaft is rigidly attached to the housing for the push/pull motor which controls the gripper. This is shown in Figure 9.

The gripper was adapted from a manipulator that is no longer functional. It is a solid aluminium with a series of one quarter inch holes drilled through the solid part of the gripper to reduce weight. The gripper weighs 2.0 pounds. A push/pull motor encased in the lower part of the gripper controls the gripper action. Figure 9 shows this assembly.

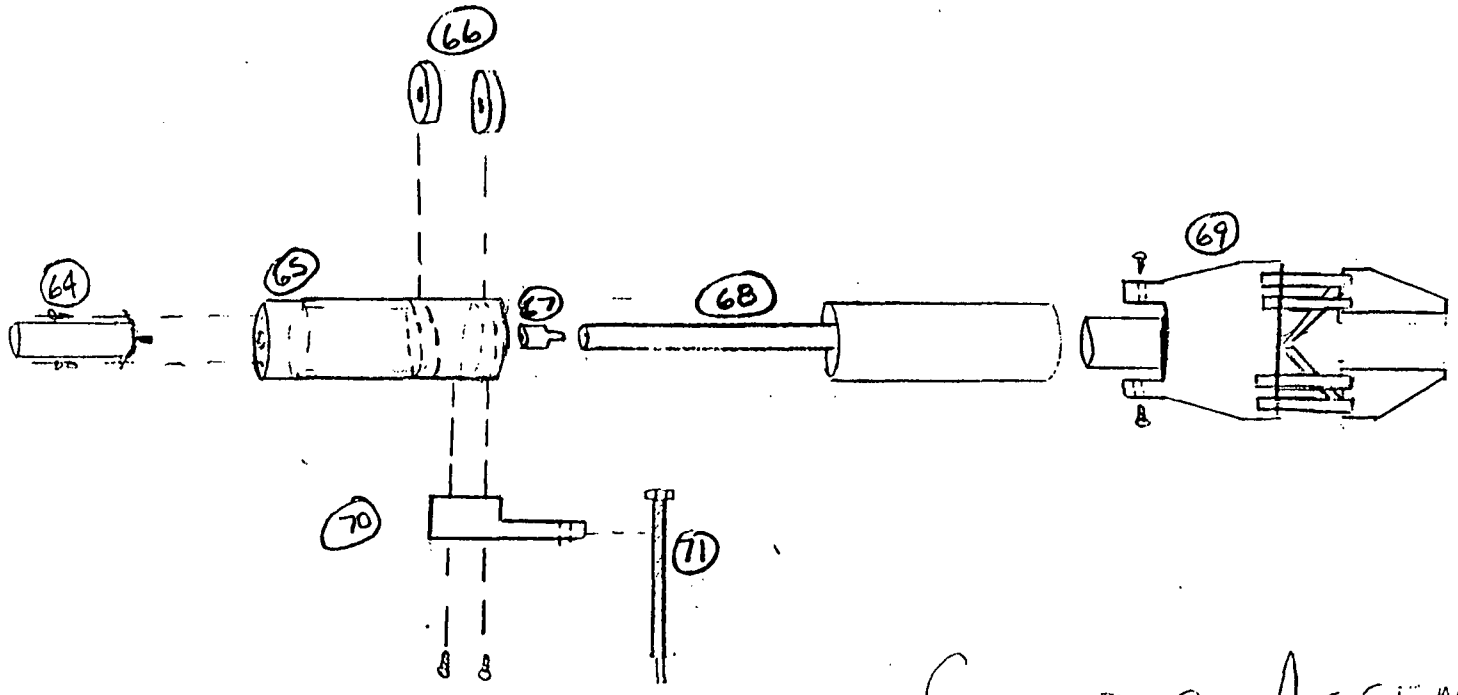

GRIPPER ASSEMBLY

KEY TO FIGURE 9

ID #	PART	SPECIFICATIONS	#
64	MOTOR	27.5 VDC DAYTOM	1
65	SUPPORTING COLLAR	1 1/2" O. D.	1
66	BEARING	1 1/4" RADIAL	2
67	CONNECTOR	1/4" COLD ROLLED STEEL	1
68	GRIPPER HOUSING	Al 6061-T6	1
69	GRIPPER ASSEMBLY	ALUMINUM AND STEEL	1

1. Manipulator Dynamics

In this section the closed form solution for the dynamics of two robotic manipulators moving a common object is developed. The approach is to develop the equations of motion for the open kinematic chain, and then close the chain through the forces applied to the common object.

Let n and m be the number of joint variables for robot manipulators 1 and 2, respectively, and define **q** as the (n+m) x 1 vector of joint variables. The Euler-Lagrange formulation of mechanism dynamics yields a set of equations that are easy to manipulate for robot control problems. The dynamic equations take the form

$$u = D(q)\ddot{q} + H(q,\dot{q}) + G(q) - J^T F$$

where,

u = **force/torque vector**

D = **manipulator mass matrix**

H = **coriolis/centrifugal force vector**

G = **gravitational force vector**

J = **end-effector Jacobian**

F = **forces applied at the end-effector**

In this formulation the equations for both manipulators are combined to form the above equation where **u**, **H**, and **G** are (n+m) x 1 vectors, and **D** and $\mathbf{J^T}$ are (n+m) x (n+m) matrices.

To put the equations of motion into a form that will be useful for path parameterization, let **w** be the vector of cartesian coordinates for the center of mass of the common object. The equations of motion of the object can then be written as

$$F = M_I(w)\ddot{w} + B(w,\dot{w}) + G_I(w)$$

where

M_I = **mass matrix of common object**

B = **object bias acceleration vector**

G_I = **object gravitational vector**

Therefore, the complete equations of motion can be written as

$$u = D(q)\ddot{q} + H(q,\dot{q}) + G(q) + J(q)^T[M_I(w)\ddot{w} + B(w,\dot{w}) + G_I(w)]$$

1.1 Parameterized Dynamics

In many robotic applications the desired path and orientation of the common object are predetermined based upon the manipulator workspace and obstacles within that workspace. When the cartesian path of the object is known, the vector w can be expressed as a function of the single scalar parameter s. This expression can be written via an analytical expression or through the use of spline functions. With the vector w known, the manipulator joint vector **q** can be described in terms of the parameter s by solving the inverse kinematics problem. Therefore, the equations of motion can be expressed as (n+m) equations in the path parameter s.

To describe the motion of the object center of mass and the joints of the manipulators the following relationships are defined

$$w = h(s)$$

$$q = f(s)$$

Differentiating with respect to time, the object and joint velocities can be written as

$$\dot{w} = h_s \dot{s}$$

$$\dot{q} = f_s \dot{s}$$

Differentiating once again, the object and joint accelerations are found to be

$$\ddot{w} = h_s \ddot{s} + h_{ss} \dot{s}^2$$

$$\ddot{q} = f_s \ddot{s} + f_{ss} \dot{s}^2$$

where the subscript s denotes partial derivatives with respect to the path parameter s, and the first and second time derivatives of s are called the *pseudo-velocity* and *pseudo-acceleration*, respectively. Using these expressions for velocity and acceleration, the equations of motion can be written in terms of the path parameter as follows

$$u = a(s)\ddot{s} + b(s)\dot{s}^2 + c(s)$$

where the (n+m) x 1 vectors **a(s)**, **b(s)**, and **c(s)** are defined as

$$a(s) = D(s)f_s + J(s)^T M_l h_s$$

$$b(s) = D(s)f_{ss} + H(s)f_s^2 + J(s)^T[m_l h_{ss} + B(s)h_s^2$$

$$c(s) = G(s) + J(s)^T G_l(s)$$

For now, the actuator torques (or forces) are assumed to be bounded by constants such that following relationship is always true

$$u_i^{\min} \le u_i \le u_i^{\max} \qquad i = 1,2,\cdots,(n+m)$$

The effects of state-dependent actuator torques can also be included in the dynamic equations; this case is discussed in section 1.2.

With the actuator bounds given, the maximum and minimum possible values for the pseudo-acceleration can be determined as functions of the path parameter and the pseudo-velocity as follows

$$u_i^{\min} \le a(s)\ddot{s} + b(s)\dot{s}^2 + c(s) \le u_i^{\max}$$

This expression can be rearranged to give a set of (n+m) constraints on the pseudo-acceleration as

$$\alpha_i \le \ddot{s} \le \beta_i$$

where

$$\alpha_i = (u_i^{\alpha} - b_i\dot{s}^2 - c_i)/a_i$$

$$\beta_i = (u_i^{\beta} - b_i\dot{s}^2 - c_i)/a_i$$

and

$$\text{if } a_i>0, \quad u_i^{\alpha} = u_i^{\min}, \quad u_i^{\beta} = u_i^{\max}$$

$$\text{if } a_i<0, \quad u_i^{\alpha} = u_i^{\max}, \quad u_i^{\beta} = u_i^{\min}$$

Therefore, the bound imposed on the pseudo-acceleration can be expressed as

$$\max[\alpha_i] \le \ddot{s} \le \min[\beta_i]$$

1.2 State-Dependent Actuator Bounds

Generally, we can assume any smooth expression for the state-dependent actuator bounds. For instance, assume that the actuators ar fixed-field dc servo motors. Then the actuator bounds take the following form

$$u_i = V_i + K_i\dot{q}_i \quad i = 1,2,\cdots,(n+m)$$

where the V_i are scaled input voltages and the K_i are constant coefficients. In parameterized form the dynamic equations become

$$V = a(s)\ddot{s} + b(s)\dot{s}^2 + d(s)\dot{s} + c(s)$$

with the vector **d(s)** defined as

$$d(s) = -Kf_s$$

and $K = \text{diag}[K_1,-,-,-K_{(n+m)}]$. The corresponding bounds on the pseudo-acceleration can now be expressed as

$$\alpha_i = [V_i^{\alpha} - (b_i\dot{s}^2 + d_i\dot{s} + c_i)]/a_i$$

$$\beta_i = [V_i^{\beta} - (b_i\dot{s}^2 + d_i\dot{s} + c_i)]/a_i$$

and

$$\text{if } a_i>0, \quad V_i^{\alpha} = V_i^{\min}, \quad V_i^{\beta} = V_i^{\max}$$

$$\text{if } a_i<0, \quad V_i^{\alpha} = V_i^{\max}, \quad V_i^{\beta} = V_i^{\min}$$

2. Minimum-Time Trajectory Planning

Minimum-time planning strategies for robot manipulators have long been a concern

in the robotics literature. Because of the nonlinear multi-input dynamics of robot manipulators, finding true minimum-time solutions is quite difficult. Earlier methods use various assumptions and simplifications on the dynamics to obtain near-minimum-time solutions. For example, Kahn and Roth [21] used linearization techniques and examined the application of linear optimal control theory. Also, purely kinematic approaches were studied by Lin, Chang, and Luh [22].

True minimum-time solutions along defined paths were derived by Bobrow, Dubrowsky, and Gibson [23], [24], Shin and McKay [25], [26], and Slotine and Yang [27]. These methods consider the full nonlinear manipulator dynamics and the actuator constraints, and therefore provide true minimum-time solutions. Each of the above studies proposed different methods of determining what are known as *switching points*. For time-optimal, path-following problems at least one of the actuators must be saturated at any time, and at the switching point there must be another actuator which is also saturated [27].

Bobrow *et al.*, and Shin and McKay suggest to find for each value of the path parameter s the maximum possible value of the pseudo-velocity to construct the so-called *maximum velocity curve* in the $s-\dot{s}$ phase plane. This corresponds to the condition

$$\alpha(s,\dot{s}) = \beta(s,\dot{s})$$

To find the point where the minimum-time phase trajectory meets the maximum velocity curve (the switching point), Bobrow *et al.*, suggests to integrate the equation $\ddot{s} = \beta(s,\dot{s})$ from the initial state until the maximum velocity curve is reached at some point a (Fig. 1), then drop to some lower velocity on the dotted vertical line, and

integrate the equation $\ddot{s} = \alpha(s,\dot{s})$ forward in time, choosing various initial values along the dotted line until the resulting trajectory just touches the maximum velocity curve at a point b.

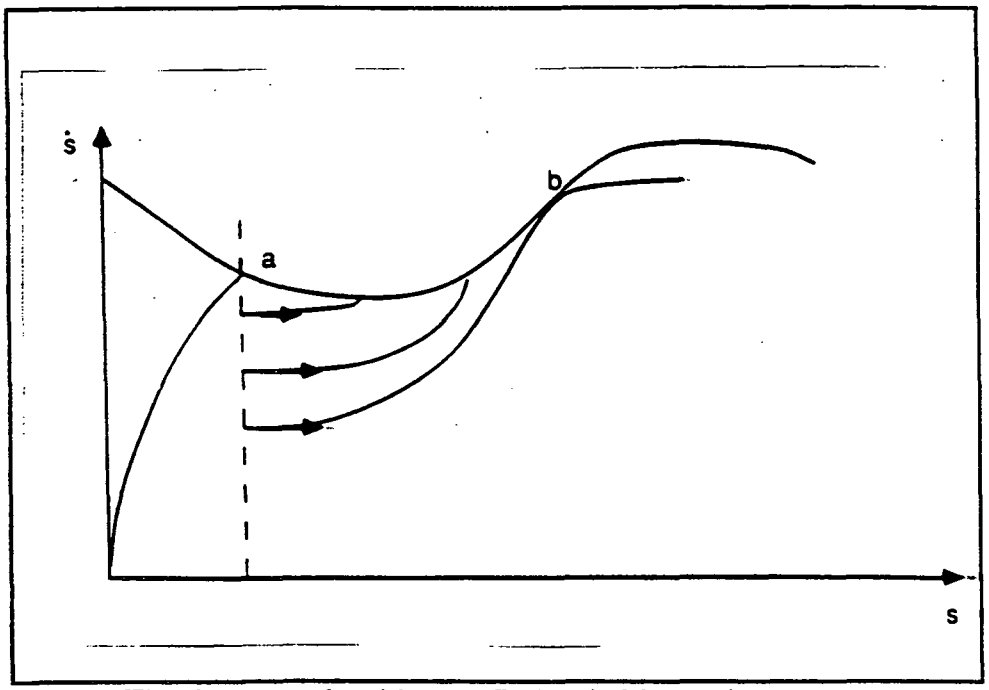

Fig. 1. The Bobrow algorithm to find switching points.

Shin and McKay have proposed a different method for finding the switching points. When the phase plane trajectory meets the maximum velocity curve, their approach is to search along the maximum velocity curve to find a point where the equation

$$\phi(s) = \frac{d\dot{s}}{ds} - \frac{dg}{ds}$$

changes sign (Fig. 2). This expression essentially determines the difference between the slope of the phase plane trajectory at the maximum velocity curve and the slope of the maximum velocity curve itself. The slope of the phase plane trajectory can be determined as follows

$$\frac{d\dot{s}}{ds} = \frac{\ddot{s}}{\dot{s}}$$

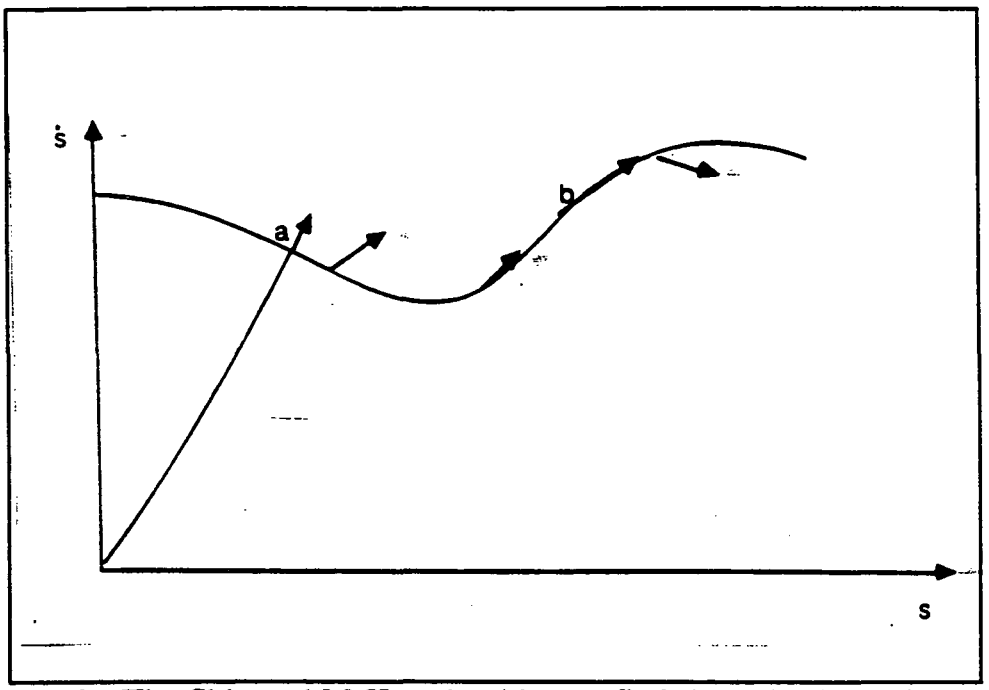

Fig. 2. The Shin and McKay algorithm to find the switching points.

Slotine and Yang have proposed a more efficient method for determining the switching points. Their method does not require the determination of the maximum velocity curve or a search over the range of possible pseudo-velocities. The efficiency of this method is that only a search over the range of the path parameter s is necessary to determine all of the possible switching points. From each of these switching points the function $\beta(s,\dot{s})$ is integrated forward in time and the function $\alpha(s,\dot{s})$ is integrated backward in time until the resulting trajectory reaches the $s=s_0$ line, the $s=s_f$ line or until an actuator constraint has been violated (Fig. 3). The trajectories formed by this integration are call the *limit curves*, under which is the admissible region for the optimal phase plane trajectory.

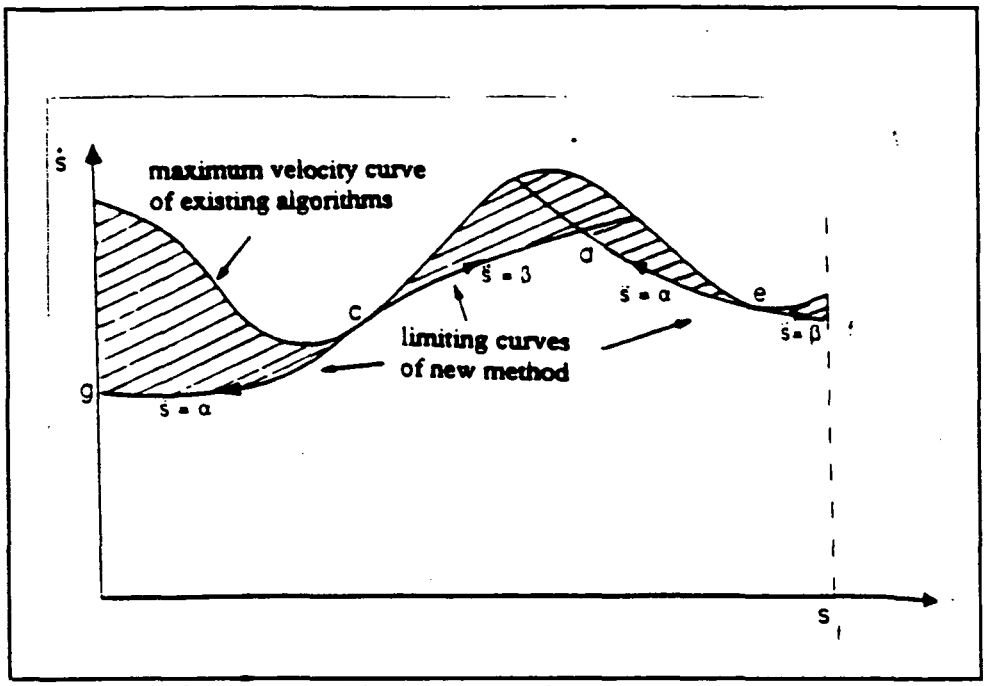

Fig. 3. The Slotine and Yang method for determining the limit curves.

All of the methods mentioned above were applied to the case of a single robot manipulator carrying no load. For *this* work the Slotine and Yang algorithm is adopted to the case of two robotic manipulators carrying a common object. The procedure of finding the switching points and limit curves remains the same, however, the dynamics of the problem are significantly changed with the interaction of carrying the common load. A complete description of the Slotine and Yang method for finding the switching points and limit curves follows.

2.1 Time-Optimal Path-Following Algorithm

As mentioned previously, the efficiency of the Slotine and Yang algorithm is that only a search over the range of the path parameter is necessary to the determine the possible switching points. In this section the various types of switching points are classified and the

methods for determining the switching point phase plane coordinates are described. The switching points are classified into three different types. They are the *zero-inertia* point, the *discontinuity* point, and the *tangent* point.

The Zero-Inertia Point

If, in the parameterized dynamic equations, $a_i(s) = 0$ for some i, then the corresponding pseudo-acceleration bounds cannot be defined. In this case the acceleration at the maximum velocity curve is not uniquely determined. The time-optimal phase trajectory may include this point and is considered a possible switching point. Since the terms in $a_i(s)$ represent inertia like terms in the parameterized equations of motion these points are called zero-inertia points. These points can be found directly from the expression of $a_i(s)$ (in the simpler cases), or through the use of the various numerical root-finding methods available.

The Discontinuity Point

In this section it is assumed that the first derivative of the parameterized path functions, namely h_s and f_s, are continuous over the entire range of s. If this is not the case at a particular point, then the velocity at this point is necessarily zero since the velocity cannot be discontinuous.

However, the second derivatives h_{ss} and f_{ss} may be discontinuous. Assume that for a given value of $\dot{s}$ the following is true

$$\alpha_m \leq \ddot{s} \leq \beta_k$$

meaning that joint m gives the maximum of decelerations and joint k gives the minimum of accelerations. At the maximum velocity limit the deceleration and acceleration bounds should be equal. For infinitesimally smaller and larger values of s in the vicinity of a given value of s, if any term in the expressions for the pseudo-acceleration changes discontinuously, then the maximum velocity curve is discontinuous in that vicinity (Fig. 4). Assuming that we do not have a zero-inertia condition, then the only terms that can possibly be discontinuous are h_{ss} and f_{ss}.

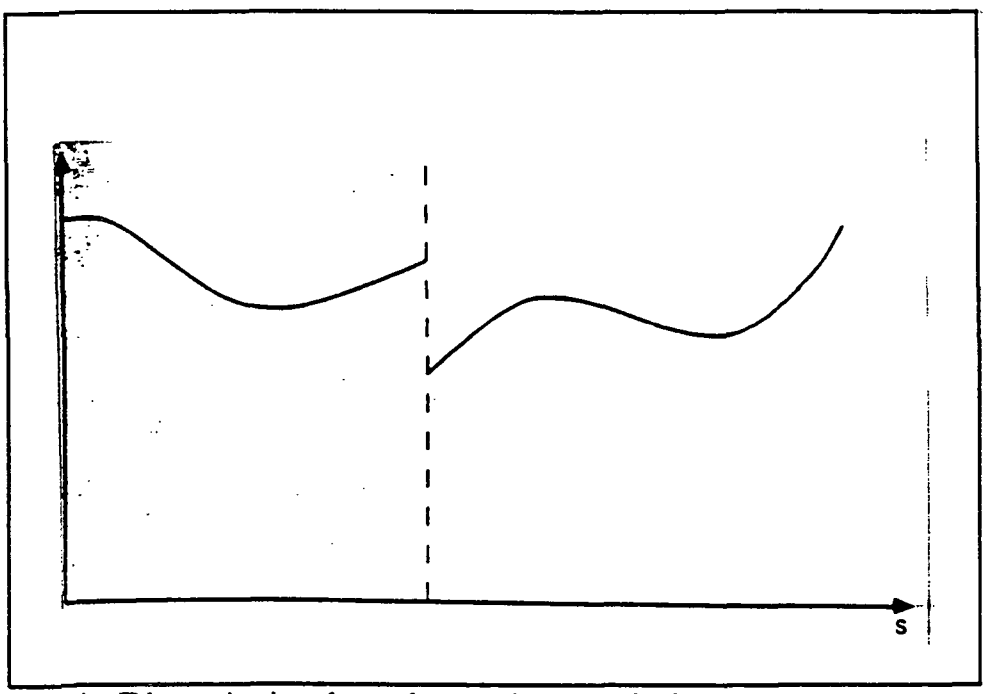

Fig. 4. Discontinuity along the maximum velocity curve.

The discontinuity points described above can be found without having to determine the entire maximum velocity curve. The values of s where hss or fss are discontinuous must be determined, and then the corresponding pseudo-velocity must be found. Using the conditions at the maximum velocity curve the possible pseudo-velocities can be evaluated as follows

$$\dot{s} = \sqrt{\frac{(a_k u_m^{\alpha} - a_m u_k^{\beta}) + (a_m c_k - a_k c_m)}{a_k b_m - a_m b_k}}$$

where this expression is evaluated for all m not equal to k. Of the possible pseudo-velocities found from this expression, the one with the least value is chosen as the possible switching point.

The Tangent Point

In this section it is assumed that for any s considered for tangent point evaluation, the zero-inertia point and discontinuity point conditions are not met. Therefore, the maximum velocity curve is both continuous and differentiable. The smoothness of the maximum velocity curve at the candidate switching point implies that the pseudo-acceleration is continuous in the region near the point. Also, the phase plane trajectory must be locally continuous and differentiable. If the phase plane trajectory meets the maximum velocity curve other than tangentially, it would enter the inadmissible region above the maximum velocity curve. Therefore, we have the condition that the phase plane trajectory must meet the maximum velocity curve tangentially.

For time-optimal path-following problems at least one of the actuators must be saturated at any time, and at the switching point there must be another actuator which is also saturated. Assume that deceleration occurs before and after the switching point with the m-th actuator saturated, the pseudo-acceleration is then given by the following expression

$$\ddot{s} = \alpha_m = [u_m^{\alpha} - b_m \dot{s}^2 - c_m]/a_m$$

and, at the switching point another torque u_k is also saturated. The torque u_k can be expressed in terms of the path parameter and the pseudo-velocity as

$$u_k = a_k[u_m^{\alpha} - b_m\dot{s}^2 - c_m]/a_m + b_k\dot{s}^2 + c_k$$

Since the pseudo-velocity is assumed to be continuous and differentiable then so must the torque u_k. If the torque trajectory meets the corresponding bound other than tangentially, the u_k would violate its constraint. Thus, the torque trajectory must meet its bound tangentially (Fig. 5).

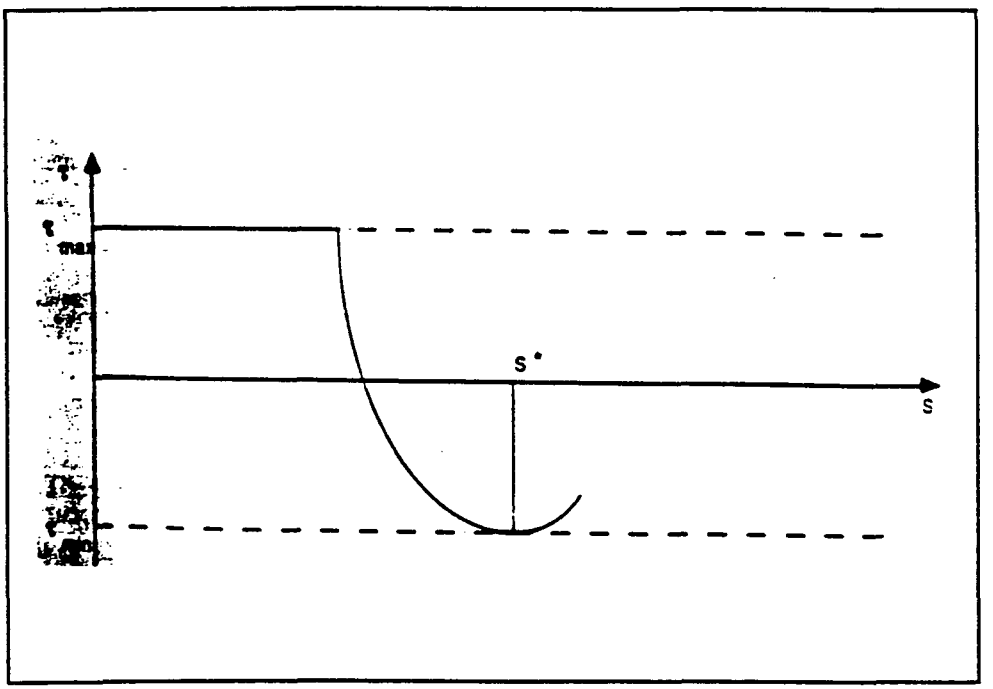

Fig. 5. Torque trajectory meeting bound tangentially.

Since the torque u_k must meet its constraint tangentially, the following condition must be true at a candidate tangent point

$$\frac{du_k}{dt} = 0$$

But this is equivalent to

$$\frac{\partial u_k}{\partial s}\dot{s} + \frac{\partial u_k}{\partial \dot{s}}\ddot{s} = 0$$

Using the expressions for the pseudo-acceleration and the torque u_k, this expression can be rewritten as

$$\phi_1(s)\dot{s}^2 + \phi_3(s) = 0$$

where

$$\phi_1(s) = \frac{d\eta}{ds} - 2\eta\frac{b_m}{a_m}$$

$$\phi_3(s) = \frac{d\rho}{ds} + \frac{d\zeta}{ds} + 2\eta\left[\frac{u_m{}^{\alpha}}{a_m} - \frac{c_m}{a_m}\right]$$

and

$$\eta = b_k - b_m\frac{a_k}{a_m}$$

$$\zeta = c_k - c_m\frac{a_k}{a_m}$$

$$\rho = \frac{a_k}{a_m}u_m{}^{\alpha}$$

Thus, for each value of s, a corresponding value of the pseudo-velocity can be found. If these two values are to define a tangent point, then the following conditions on the torques must be satisfied. If the torque u_k equals its minimum or maximum bound (depending on the sign of a_k) and the other torque constraints are satisfied then a possible tangent point

has been found. It should be noted that the d/ds terms in the tangent point equation are generally difficult to evaluate analytically, however, they can be appropriately approximated using numerical techniques.

2.2 State-Dependent Actuator Bound Effects on Switching Point Determination

Obviously, there is no effect on the determination of any zero-inertia points due to the use of state-dependent actuators, however, the determination of the discontinuity points is effected, and the tangent point search is significantly effected. Specifically, the discontinuity point search is altered since the expression for the pseudo-velocity is now written as the quadratic equation

$$(a_m b_k - a_k b_m)\dot{s}^2 + (a_m d_k - a_k d_m)\dot{s} + (a_k V_m^{\beta} - a_m V_k^{\alpha}) = 0$$

Again, this expression should be evaluated for all k not equal to m, and the smallest positive value for the pseudo-velocity use as the switching point.

Regarding the tangent point search, the pseudo-acceleration expression is now

$$\ddot{s} = [V_m^{\alpha} - (b_m\dot{s}^2 + d_m\dot{s} + c_m)]/a_m$$

and the expression for the scaled voltage V_k is

$$V_k = a_k[V_m^{\alpha} - (b_m\dot{s}^2 + d_m\dot{s} + c_m)]/a_m + b_k\dot{s}^2 + d_k\dot{s} + c_k$$

The tangentially condition is essentially the same, namely that the time derivative of V_k is equal to zero. This results in the following condition for determining the possible pseudo-velocities

$$\phi_1(s)\dot{s}^3 + \phi_2(s)\dot{s}^2 + \phi_3(s)\dot{s} + \phi_4(s) = 0$$

where

$$\phi_1(s) = \frac{\partial \eta}{\partial s} - 2\eta \frac{b_m}{a_m}$$

$$\phi_2(s) = \frac{\partial \sigma}{\partial s} - 2\eta \frac{d_m}{a_m} - \sigma \frac{b_m}{a_m}$$

$$\phi_3(s) = \frac{\partial \rho}{\partial s} + \frac{\partial \zeta}{\partial s} + 2\eta \left[\frac{V_m^{\alpha}}{a_m} - \frac{c_m}{a_m} \right] - \sigma \frac{d_m}{a_m}$$

$$\phi_4(s) = \frac{\zeta}{a_m} (V_m^{\alpha} - c_m)$$

and

$$\sigma(s) = d_k - d_m \frac{a_k}{a_m}$$

For the case of state-dependent actuator bounds inadmissible regions or "islands" may occur in the phase plane (Fig. 6). Which means that the tangentiality expression yields multiple positive solutions. Based on previous arguments regarding the necessary actuator trajectory conditions, the tangentiality condition must hold on the boundary of the islands. The solution of the cubic tangentiality equation for the pseudo-velocity can readily be found using numerical root-finding techniques. Also, a check of the scaled voltage bounds is required to determine the tangent points (as opposed to torque bounds in section 2.1).

2.3 Minimum-Time Algorithm

Based on the above discussion the minimum-time trajectory planning algorithm can be summarized as follows:

1.) Using the switching point search methods described, determine all of the candidate switching points by searching over the values of s. Note that if the tangent point condition is satisfied over a finite region, then the phase plane trajectory coincides with the maximum velocity curve in that region.

2.) Integrate forward and backward in time from each of the candidate switching points to construct the limit curves. If integration cannot be performed (forwards or backwards) without violating actuator constraints then the switching point should be discarded.

3.) Integrate forward from the initial state and integrate backward from the final state until the limit curve is met to construct the complete optimal trajectory.

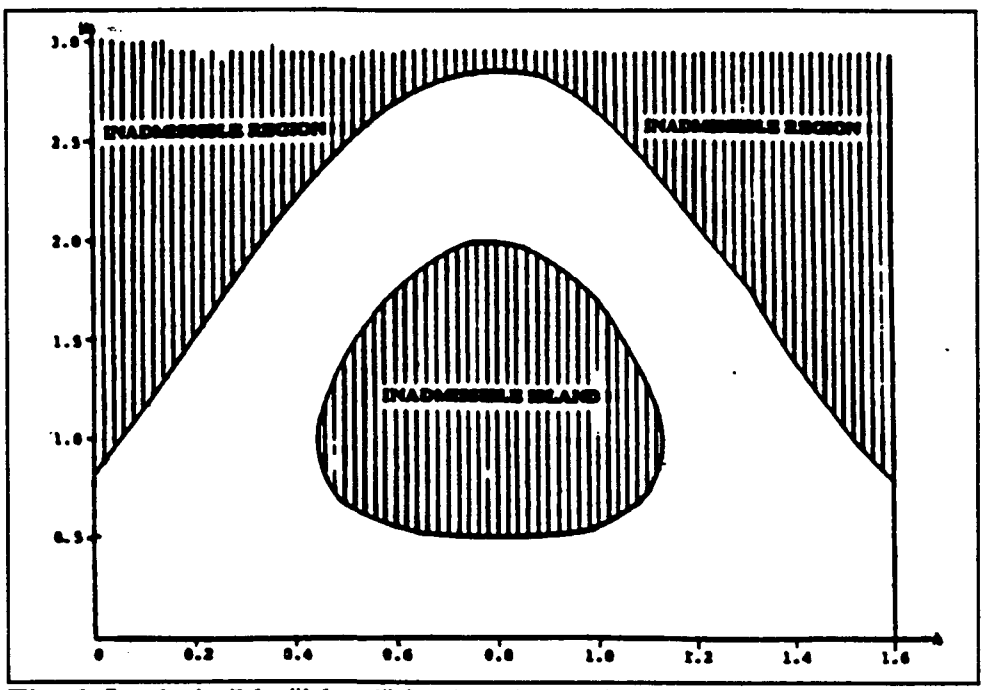

Fig. 6. Inadmissible "island" in the phase plane.

3. Minimum-Energy Trajectory Planning

For the time-optimal problem we knew that at least one of the joint actuator torques must be saturated at any given time. This was a key condition that enabled the use of the switching point methods outlined in section 2. However, in general, minimum-time does not necessarily mean minimum-cost, and for these problems there may or may not be a saturated torque at a given time. Therefore, the switching point methods cannot be used

in the general minimum-cost problem. For minimum-cost problems the dynamic programming approach, which minimizes a particular performance index (or cost function), has been studied and applied to robotic manipulator trajectory planning.

Singh and Leu [28] applied the dynamic programming method to a path-tracking robotic manipulator. They solve the problem by discretizing the cartesian path followed by the end-effector and using the kinematic solution to generate discretized joint trajectories. Jouaneh, Dornfield, and Tomizuka [29] applied the same method to the coordination of a robotic manipulator and a positioning table. Shin and McKay [30] employed the dynamic programming approach in the phase plane by using the parameterized dynamic equations.

For this work, we will use dynamic programming to solve the minimum-energy trajectory planning problem for coordinated manipulators. The problem is handled in the phase space and the use of the parameterized dynamic equations derived in section 1. A complete description of the dynamic programming algorithm follows.

3.1 Dynamic Programming

Dynamic programming is a multi-stage optimization technique where the decisions are made sequentially over time. The problem to be optimized is broken down into steps, or stages, and one or more variables is identified as the state variable for which the optimal solution is sought. At each stage a set of admissible state variables is formed from a set of possible state variables. For each state variable in the admissible set, the performance index is determined and is used to select the optimal value of the state variable. Finally, the results from each stage are combined to generate the complete solution to the problem.

The dynamic programming method can handle various types of optimization problems

depending on the specific performance index that is used. In general form, the performance index is defined as

$$J = K(q(t),t) + \int_0^{t_f} L(q(t),u(t))dt$$

The performance index for energy-minimization problems is expressed as

$$J = \int_{q_o}^{q_f} u^T dq$$

For discretization purposes the performance index can be put in the following summation form

$$J = \Sigma u^T \Delta q$$

Specifically, for the parameterized path problems addressed in this work, the path is discretized into N intervals (small enough such that the terms in the parameterized equations do not vary significantly), and the pseudo-velocity is chosen as the state variable over which the dynamic programming search is conducted. In other words, for each value of s, the pseudo-velocity range is discretized and from this discretized set the admissible set of velocities is formed. Let k be the index of the discrete points along the parameterized path, and consider the common object travelling from point k to k+1. For a possible pseudo-velocity at point k and an admissible pseudo-velocity at point k+1 the pseudo-acceleration is

$$\tilde{s}_k = \frac{[\dot{s}_{k+1}]^2 - [\dot{s}_k]^2}{2[s_{k+1} - s_k]}$$

which is considered constant over the interval. Using the possible pseudo-velocity and the corresponding pseudo-acceleration at point k, the actuator torques can be found from the parameterized equations of motion. If any of the calculated torques exceeds its actuator constraints then the possible pseudo-velocity is inadmissible. If the calculated torques satisfy the corresponding constraints then the possible velocity is added to the set of admissible velocities at point k.

Let C_k denote the incremental performance index from points k to k+1 and J^o_k denote the minimum performance index to reach the final state from the state at point k. Then, applying Bellman's optimality principle [31] yields

$$J^o_k = \min[C_k + J^o_{k+1}]$$

This equation applies to every admissible pseudo-velocity at point k. Therefore, for each admissible velocity at point k, a unique optimal velocity at point k+1 can be identified. The optimization process is achieved by starting from the final state and proceeding backwards to the initial state. This is shown graphically in figure 7 where the admissible velocity at point m has an optimal velocity pointer set to point p in the previous step.

3.2 Minimum-Energy Algorithm

Based on the above description, the algorithm for minimum-energy trajectory planning can now be stated.

1.) Discretize the parameterized path to be followed by the common object into N segments (a total of N+1 points).

2.) At each discretized point determine the joint displacements by solving the inverse kinematic equations.

3.) Let $J^o=0$ and k=N-1.

4.) Discretize the pseudo-velocity range at point k into a set of possible velocities. Initially, set the list of admissible velocities to be the same as the set of possible velocity list. For a possible pseudo-velocity at point k and an admissible pseudo-velocity at point k+1, determine the pseudo-acceleration and the required torques to move from point k to k+1. If any of the computed torques exceed its corresponding bound, then exclude this possible velocity from the admissible list.

5.) For each admissible pseudo-velocity at point k, compute the incremental performance index between points k and k+1.

6.) Using the Bellman optimality principle, determine the optimal pseudo-velocity at point k+1, which minimizes the performance index from the state at point k to the final state at k=N. Set a pointer from the pseudo-velocity at k to the optimal velocity at k+1.

7.) Repeat steps (4) to (6) for k=N-2 to k=0. When K=0, the initial state has been reached, and the optimal path has been obtained.

8.) March forward in time from the initial state to the final state using the pointers to obtain the optimal sequence of pseudo-velocities. From the optimal sequence of velocities the pseudo-accelerations and joint torques can be computed.

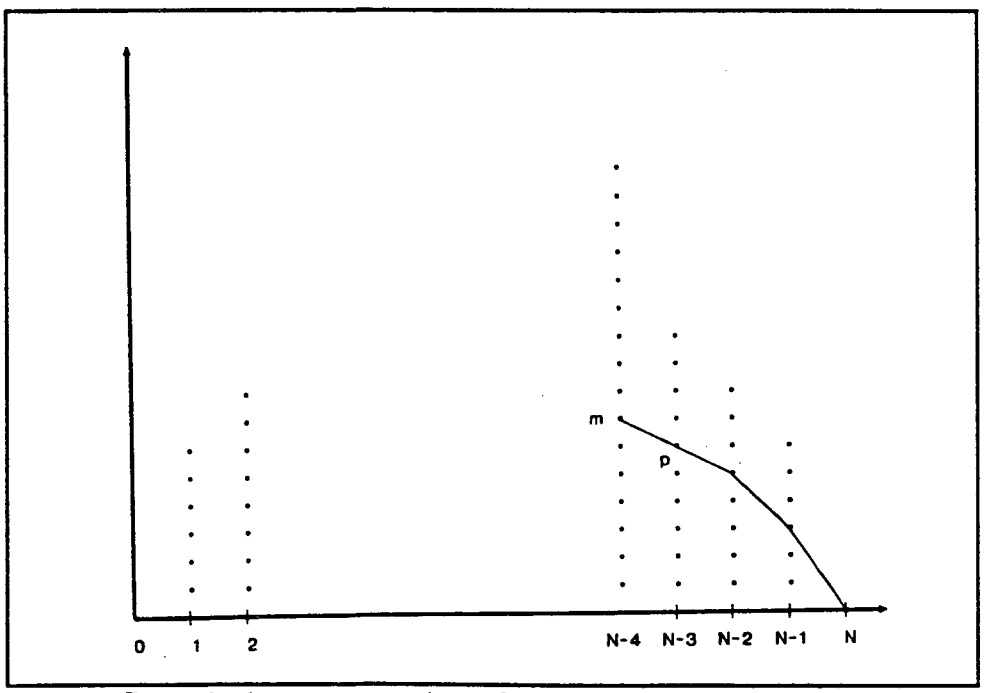

Fig. 7. Graphical representation of dynamic programming method.

The accuracy of the solution given by this algorithm depends on the resolution of the pseudo-velocity discretization. Increasing the number of discretizations makes the accelerations between stages smaller, ensuring that more possible velocities are included in the admissible list. If M_k is the number of velocity discretizations at point k and M_{k+1} is the number of discretizations at point k+1, then, in the worst case, the algorithm would have to go through M_k x M_{k+1} searches to define an admissible velocity set at point k. This defines the worst case since the possible set of M_{k+1} velocities will, generally, have been reduced in the previous step.

4. Application of Algorithms

To demonstrate how the path plannig algorithms work, they will be applied to a numerical example. The configuration of this example is shown in figure 8. While this is a relatively simple configuration it provides an adequate problem for the application of the algorithms.

For the model configuration shown in figure 8, the manipulator links have unit mass (kg) and unit length (m), while the common object has a mass of 0.25 kg with a length dimension of 0.25 m and a height dimension of 0.1 m. The distance between the bases of the manipulators is 2.0 meters. The parameterized vector of cartesian coordinates for the object center of mass is

$$w = h(s) = \begin{bmatrix} \frac{1}{2}[s - .5]^3 + \frac{17}{16} \\ \\ \frac{1}{2}s \end{bmatrix}$$

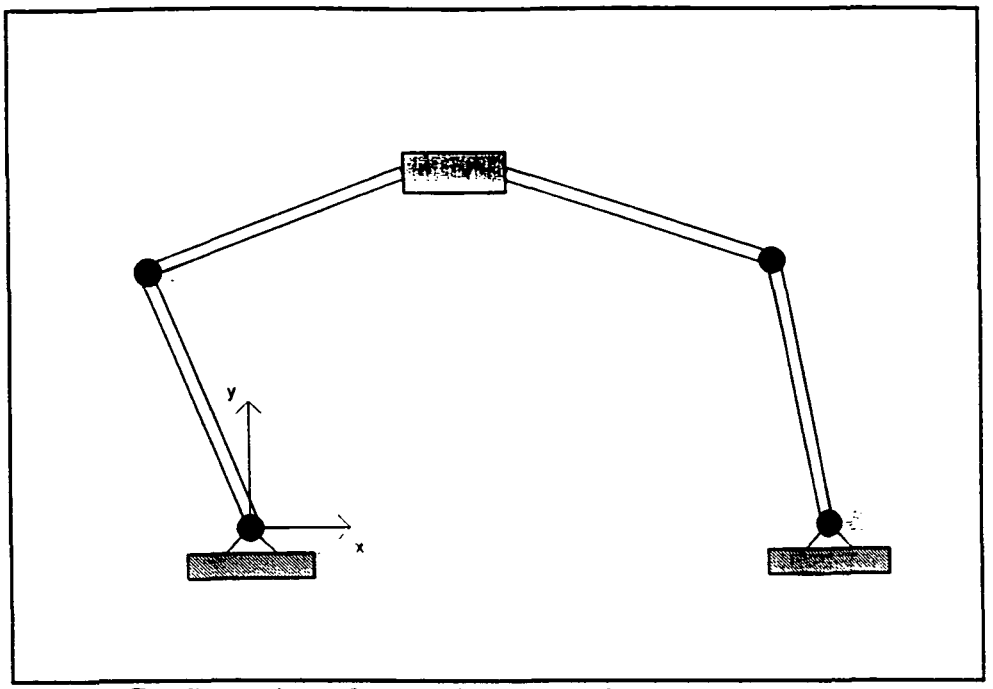

Fig. 8. Configuration of numerical example.

The cartesian path of the common load is shown in figure 9.

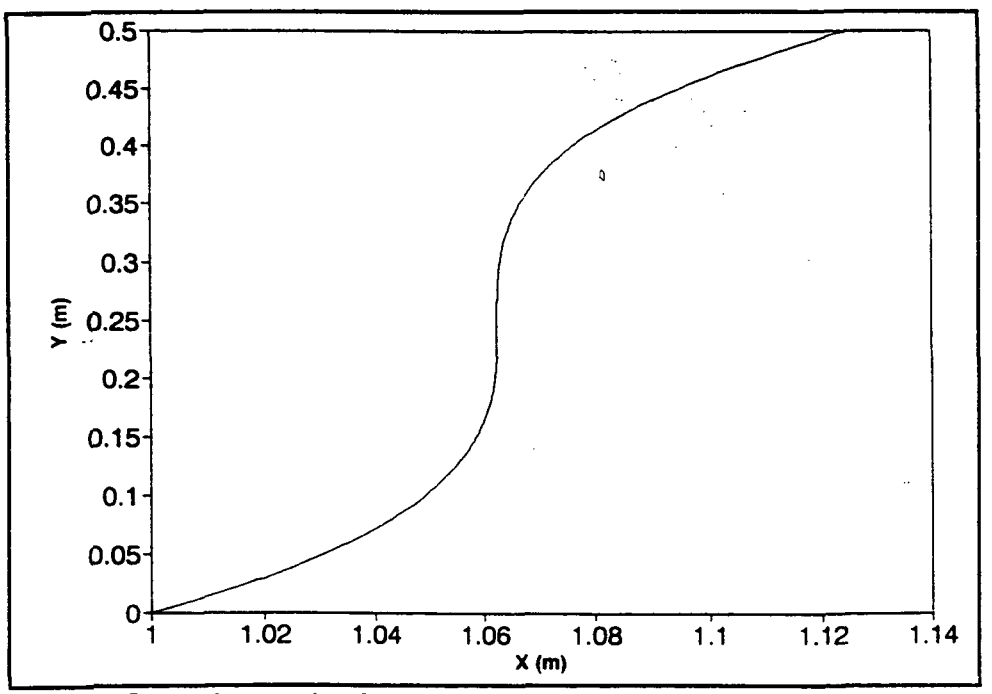

Fig. 9. Cartesian path of common object.

The orientation of the common object is chosen to remain constant throughout the range of motion. Therefore, the angular velocity and acceleration of the object is alwarys zero.

Based on the given path of the object, the parameterized joint displacements can be found by solving the inverse kinematic equations. The analytical form of these equations are quite cumbersom but the results are presented graphically in figure 10.

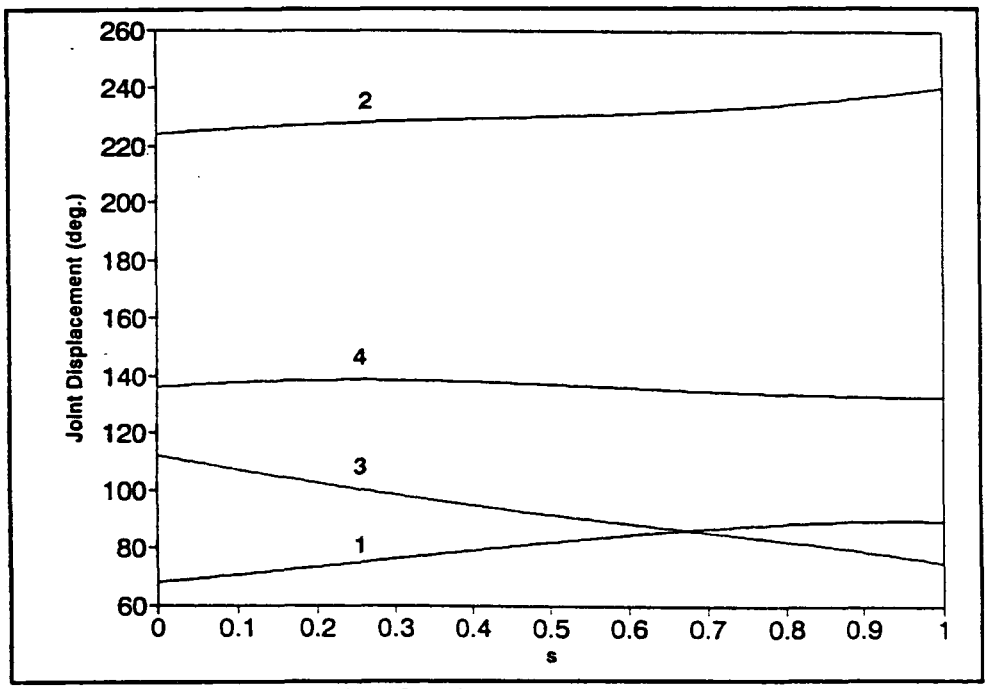

Fig. 10. Kinematic solution for the parameterized joint displacements.

Finally, the actuator constraints must be defined. The joint force/torque bounds obviously depend on the type of servo motors used. These must be chosen such that the force/torques are more that "strong" enough to move the manipulators to any position and be able to statically hold that position. For this example the actuator constraints are chosen to be constant and defined as

$$-30 \text{ N-m} < u_1 < 30 \text{ N-m}$$

$$-20 \text{ N-m} < u_2 < 20 \text{ N-m}$$

$$-35 \text{ N-m} < u_3 < 35 \text{ N-m}$$

$$-15 \text{ N-m} < u_4 < 15 \text{ N-m}$$

4.2 Minimum-Time Path

Following the algorithm outlined in section 2, the candidate switching points must be identified. Examining the the cartesian path we can see that there are no discontinuity points. By carrying out a search over the values of s, two zero-inertia points are found. The inertia term a4 becom zero at the phase coordinate (0.2634, 5.956), and the term a1 becomes zero at (0.9337, 6.098). The tangent point search produces a possible switching point at the coordinate (0.8, 6.968).

With the candidate switching points found the next step is to integrate the pseudo-acceleration bounds forward and backward from each point. This was performed using a second order Adams-Bashforth integration scheme. The resulting limit curves are shown in figure 11. Figure 12 shows the same limit curves with the maximum velocity curve superimposed demonstrating how the limit curve decrease the area of admissibility.

The final step in constructing the time-optimal path is to integrate forward from the initial state and backward from the final state to form the accelerating and decelerating "legs" of the optimal trajectory. The results of this integration complete the optimal path and are presented in figure 13.

For completeness, the torque history is presented figure 14. Notice in this figure how at any given time at least one of the actuator torques is saturated and that the discontinuous changes occur at the switching points.

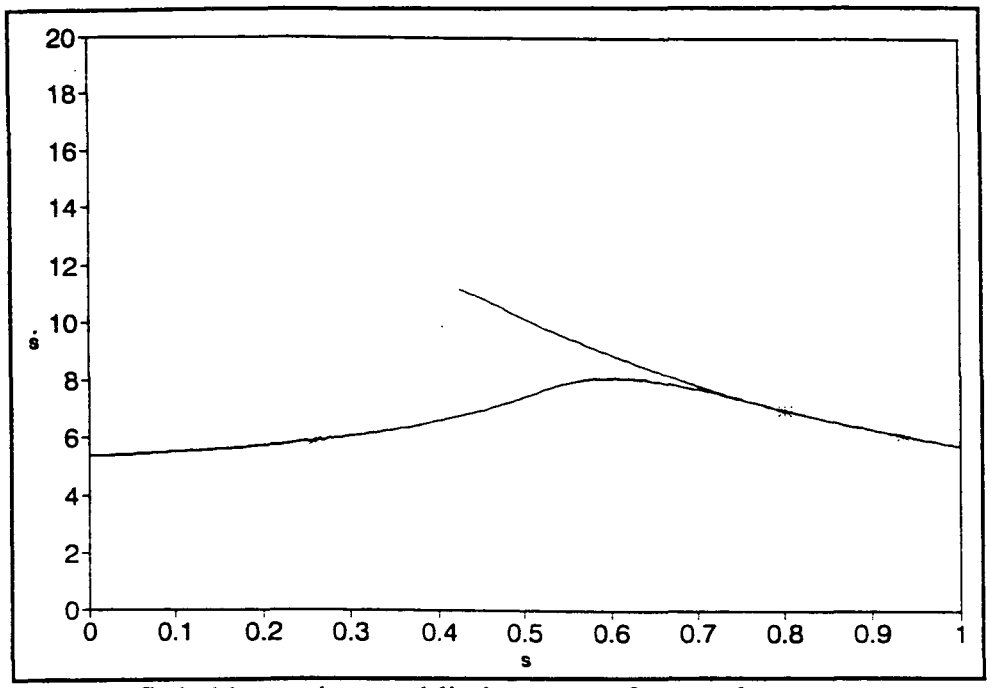

Fig. 11. Switching points and limit curves of example.

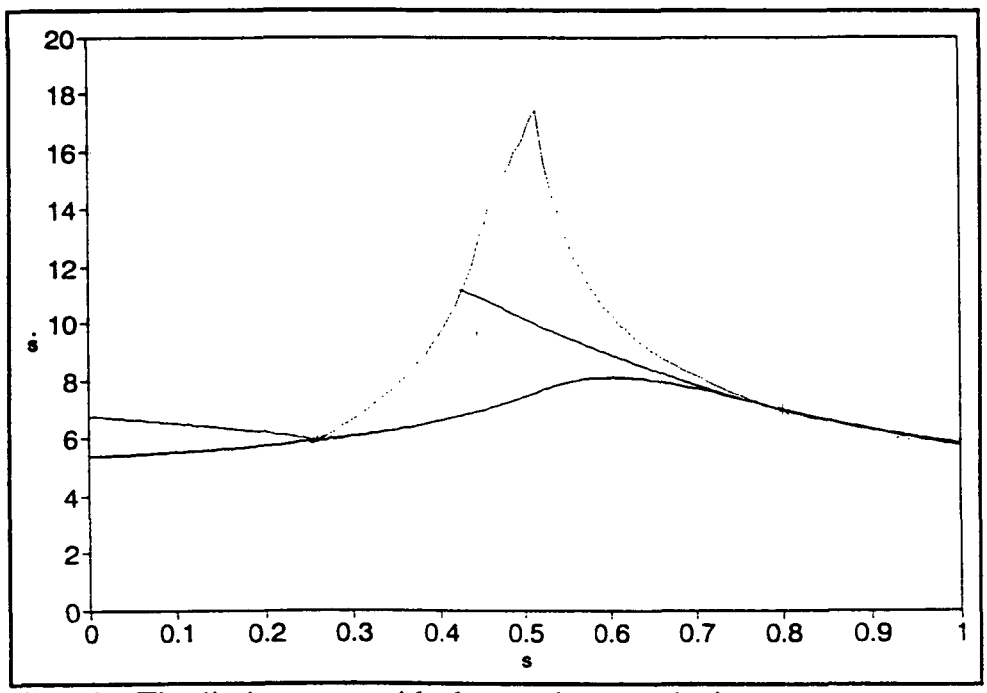

Fig. 12. The limit curves with the maximum velocity curve.

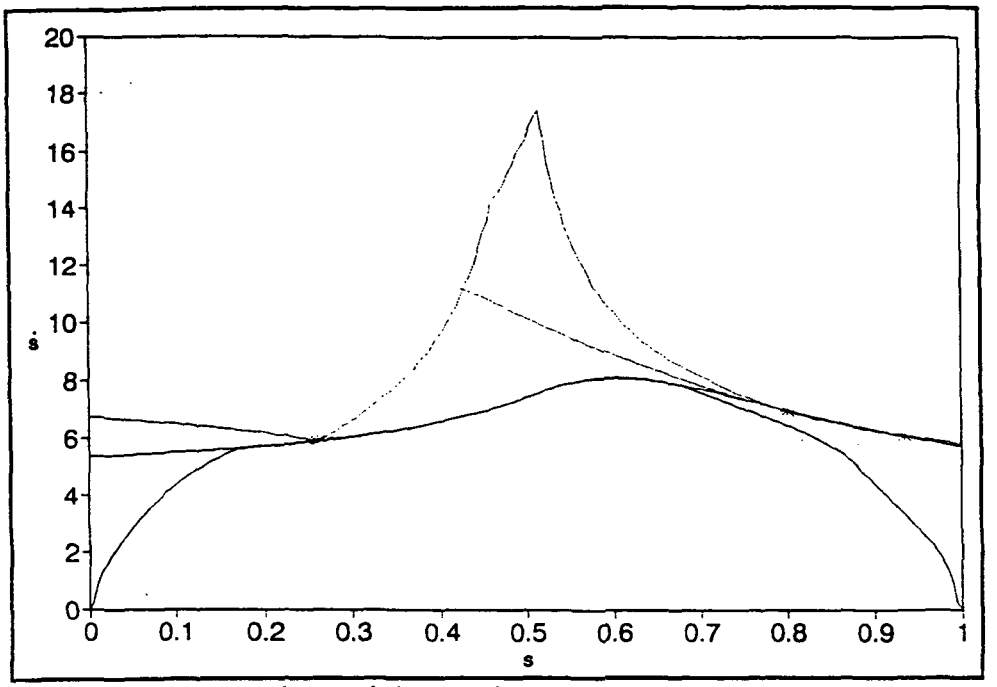

Fig. 13. The complete minimum-time trajectory.

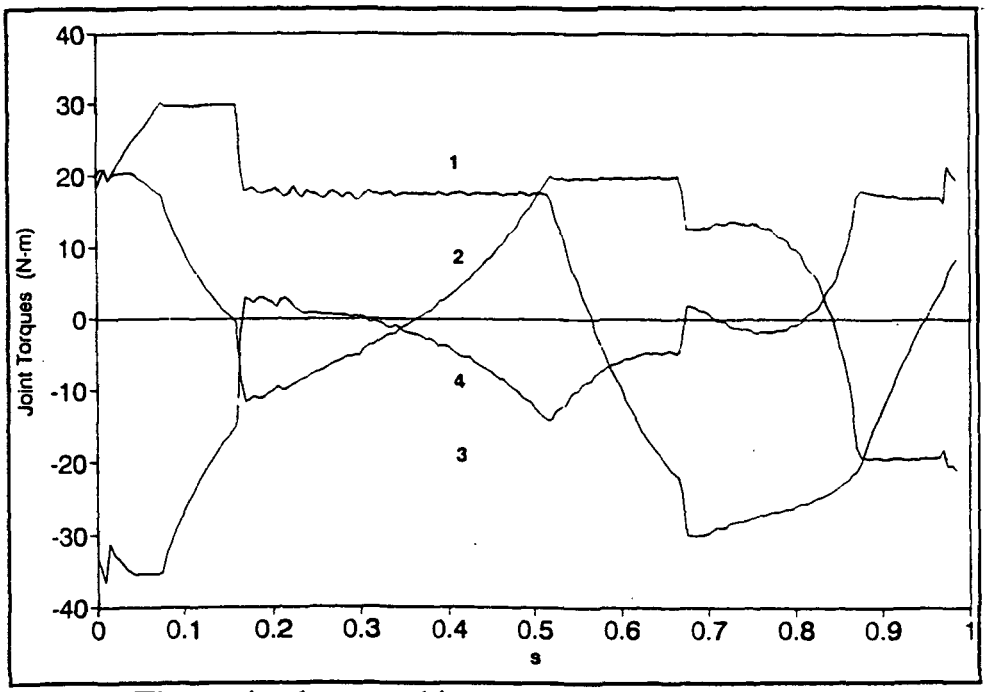

Fig. 14. The optimal torque history.

4.3 Minimum-Energy Path

To set up this example for the minimum-energy algorithm, the range of s was discretized into increments of 0.01. In other words, 101 discrete points (N=101) and 100 intervals. The possible pseudo-velocity range was discretized into 201 discrete points in increments of 0.005 at each discrete point s_k. Following the algorithm outlined in section 3, the minimum-energy phase trajectory was determined (fig. 15). The maximum velocity curve is included in the figure as a reference. Again, for completeness, the torque history is presented in figure 16. Notice in this torque history none of the actuators becomes saturated at any time during the motion. Figure 17 is included to compare the time-optimal and energy-optimal trajectories.

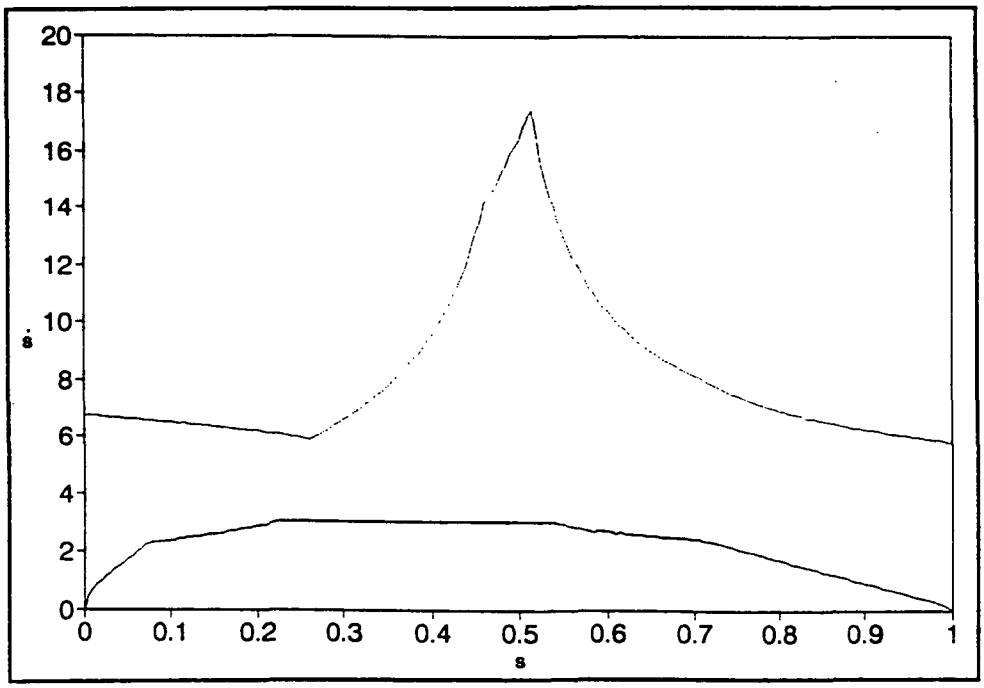

Fig. 15. Minimum-energy phase trajectory.

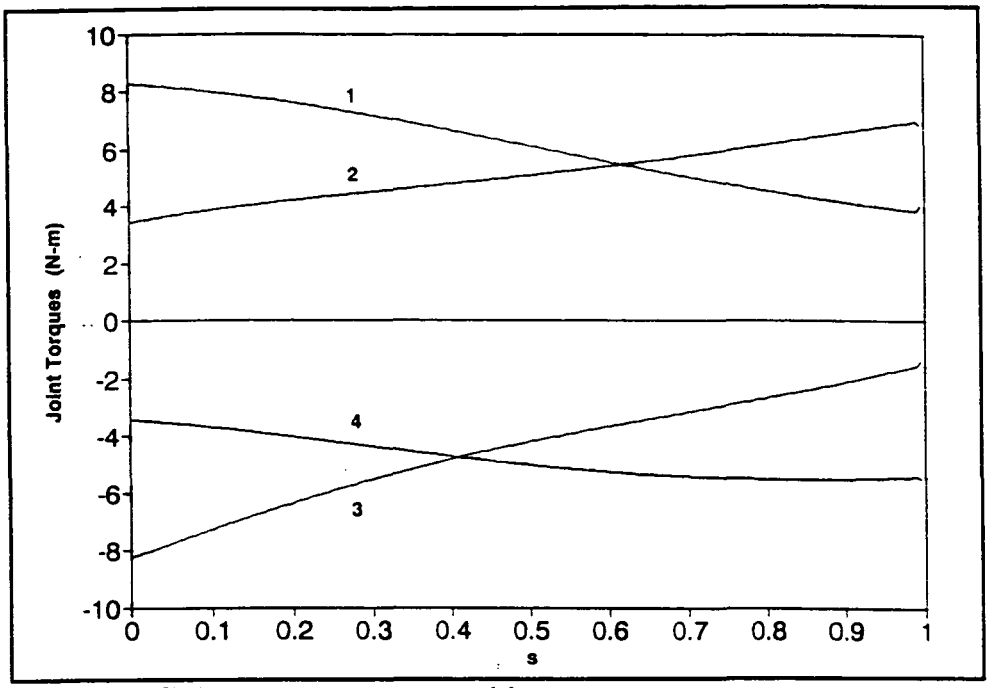

Fig. 16. Minimum-energy torque history.

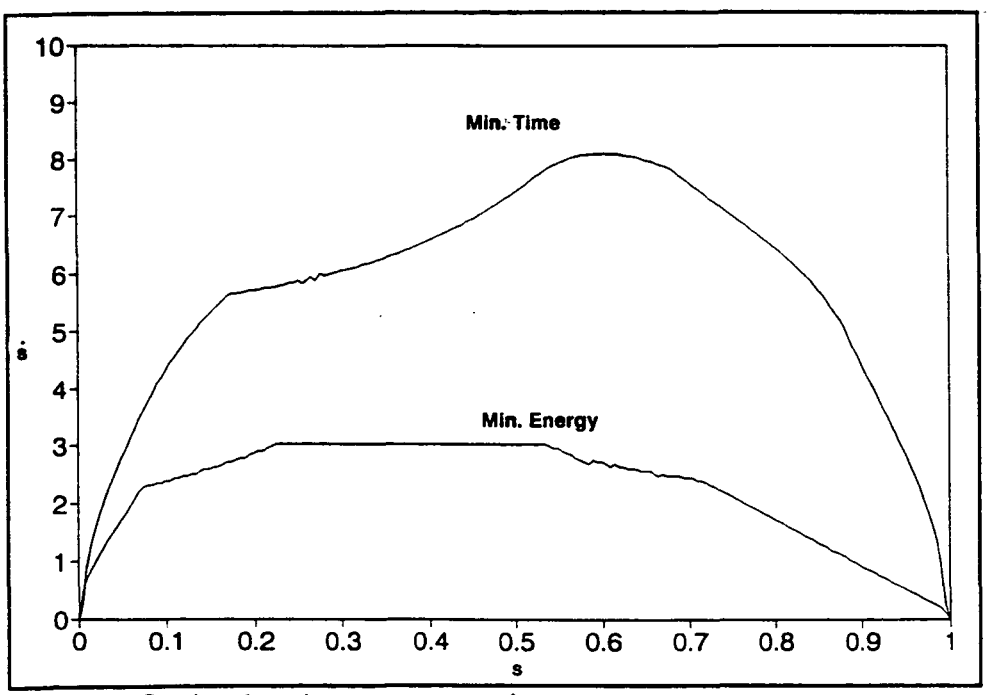

Fig. 17. Optimal trajectory comparison.

TELEMETRY

The telemetry system for the ASPOD is designed to control the robotic arm, and to simulate the future operation of the system in space. A few telemetry subsystem considerations that should be accounted for in this system are:

* A duplex communication link (i.e. a transmitter and a receiver at both remote and local sites).
* A self contained power source for the system on the remote end.
* System should operate in real time.
* Redundancy (for space application).

Taking these factors into account, a Radio Modem and a Photonic telemetry system were chosen for evaluation.

Telemetry Systems

The Radio Modem telemetry system (shown in Figure 10) is composed of a lap-top IBM PC connected to a transceiver (radio modem) and an interface at the remote site. At the local (user) site an IBM PC is connected to a transceiver. The computers are linked to the modems with an RS-422 serial port.

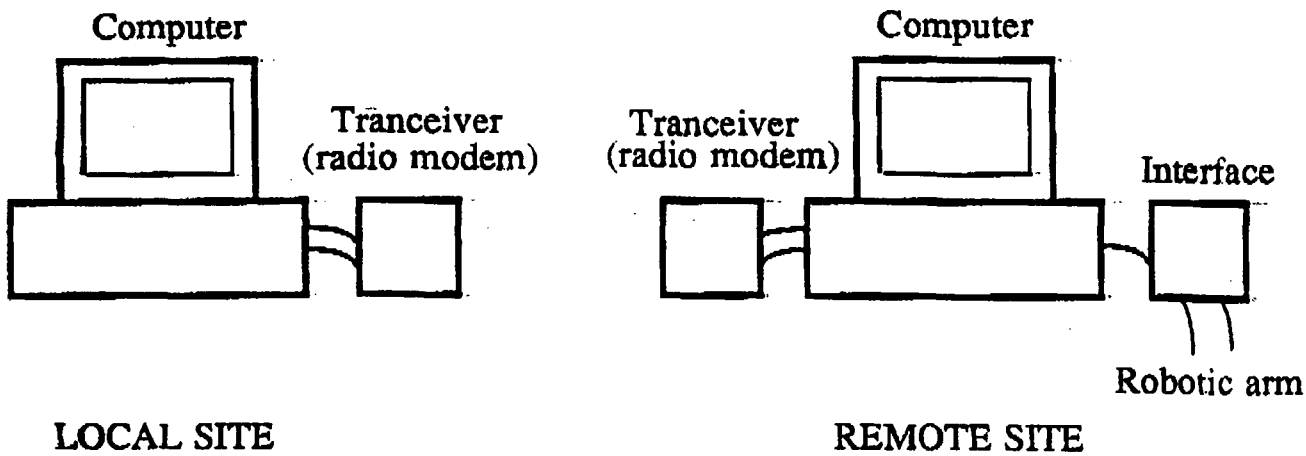

Figure 1 1991-1992 RADIO MODEM TELEMETRY SYSTEM

To simulate the telemetry system to be used in space, a self-contained power source (for the remote site) has been proposed.

Wires wil be connecting the computer and modem, the computer and interface, and the power source to the computer and modem. This power source is proposed to use solar energy.

Likewise, the Photonic telemetry system uses local resources to operate. This system is an optically pulsed powered sensor system which converts an incoming optical pulse (or a series of pulses) to a voltage by an array of photovoltaic cells. There is no external power source required for the (remote) sensing end. This system improves the performance of the conventional two-wire electronic telemetry system because there are fewer electric components, and as a result less heat is dissipated. Additionally, this system isolates the electric components which reduces the electromagnetic interference (EMI) between links of the beam.

Both the Radio Modem Optical Link telemetry systems have duplex communication links, a self-contained power source (for the remote end), and operate in real time. Redundancy could be applied, but is only needed for space application. Nevertheless, there are disadvantages of each of these systems. A direct line of sight must be maintained for both systems. This requirement is not as strict for the Radio Modem telemetry system as for the Photonic telemetry system. However, once a direct line of sight is achieved for the laser, the signal is accurate and reliable, while communication signals through radio frequency (RF) waves will fade occassionally (throughout the month) due to sunspots.

ASPOD Telemetry System

The Radio Modem telemetry system will be used for ground application on the ASPOD project. It will still simulate space operation by having a self-contained power source and radio frequency (RF) shield (for each part of the system) to block out radio frequency interference (RFI). However, the Photonic telemetry sytem should be incorporated into the future design for space application. The final system will need a radiation shield to minimize RFI.

SOLAR TRACKER

A solar tracking system was designed on the basis of utilizing a local resource, the sun's energy, to cut orbital debris. In order for this system to work effectively as well as efficiently, the Autonomous Space Porcessor for Orbital Debris (ASPOD) solar cutter must be directly aligned with the sun (in elevation and azimuth) to obtain a maximum amount of solar energy. This alignment is required in order to cut materials when using focused light for the reason that energy must be input to a point faster than it can be conducted, convected, reflected, emitted, or re-radiated away [1]. The solar tracking system is composed of 2 directional systems (one for elevation and one for azimuth), and a control box. Within each of the directional is a mounted gear train apparatus, a 90-VDC motor and a pair of solar photovoltaic cells.

Solar Photovaltaic Cells

The solar photovoltaic cells are arranged in right-angled configurations as shown in figure 1. These sensors are mounted on the ASPOD (see figure 2) with the bisector of the angle between the cells perpendicular with the focal axis of the solar cutter. Depending on which solar cell is receiving the most solar flux, a voltage difference (positive or negative) will result. However, if the solar flux is of equal intensity on each solar cell, the voltage difference will be zero. This voltage output is sent to the control box which then a signal to the servo motor. Note, the two directional systems are independent of one another.

The voltage difference is related to the direction of the solar tracker in the following manner: If the voltage difference across the solar cells is zero, the solar tracker is in direct alignment with the sun. If there is a positive or negative voltage difference, then the tracker is leading or lagging the sun.

Control Box

The control box (see Figure 3) is designed to align the solar tracker with the sun. This tracking can be accomplished both manually and automatically. When operating the solar tracker an important consideration to be taken into account is: ALWAYS keep the speed dial on low when starting operation. This includes the transition from manual mode to the sensor mode and when switching direction, CW or CCW, (in either sensor or manual mode).

OPERATING INSTRUCTIONS FOR THE CONTROL SYSTEM OF THE ASPOD PROJECT

GENERAL SAFETY INFORMATION

Important information to reduce the risk of electric shock and destruction of the control box.

1. Controller housing (box) must be properly grounded.
2. Disconnect power supply before servicing or removing components.
3. At no time should circuit continuity be checked by shorting terminals with a screwdriver or other metal device.
4. Do not place controller where ambient temperature is outside of the range of -10 C(15 F) to 45 C(115 F).

OPERATION

These instructions correspond with ground (testing) operation of the solar tracker (ASPOD Project)

CAUTION: THIS ADJUSTABLE SPEED CONTROLLER IS DESIGNED TO OPERATE FOR A 90 VDC MOTOR.

WARNING: DO NOT OPERATE THE CONTROLLER IN A DUSTY OR WET ENVIRONMENT. IT IS NOT SEALED FOR THIS KIND OF PROTECTION.

Note: If the solar tracker is already aligned with the sun, skip to step 7. If not proceed below:

1. Turn Speed Control dial to zero (fully CCW).
2. Set Control Mode switch to manual control.
3. Set Direction switch to adjust solar tracker in the sun's direction (CW or CCW).
4. Turn on the main power switch.

Note: if the solar tracker is moving the wrong way (away from the sun), turn off the power and set the direction switch the other way.

** **IMPORTANT** The speed dial must be at a low setting when changing direction.

5. Set Speed switch to on position.

6. Let the motor run until the solar tracker is close to being aligned with the sun.

7. Set the Speed switch to the brake position. Turn the speed dial low (fully CCW).

8. Set the Control Mode switch to sensor control.

9. Turn on the Sensor Power switch.

10. Adjust the Speed Control dial to approximate the speed of the sun moving across the sky. This will change depending on the time of year. The speed is adjusted properly if the motor is running smoothly. If the speedpot setting is too low the solar trackers will be lagging the sun constantly trying to catch up. However, if it is set too high the solar tracker will constantly be fluctuating from leading then lagging (and vice versa) the sun.

When the sensor mode is on, the direction corresponds to voltage differences, not CW or CCW settings. If the tracker is moving in the wrong direction, the positive and negative connections on the solar cells may need to be switched (Note: Turn the power switch off before changing connections). The block diagram of the system is shown in Figure 5.

Inside the Control Box:

When operating in the sensor mode, relays are used to align the tracker with the sun. The relays use the positive or negative voltage difference (given by the solar flux) to determine the corresponding direction (CW or CCW).

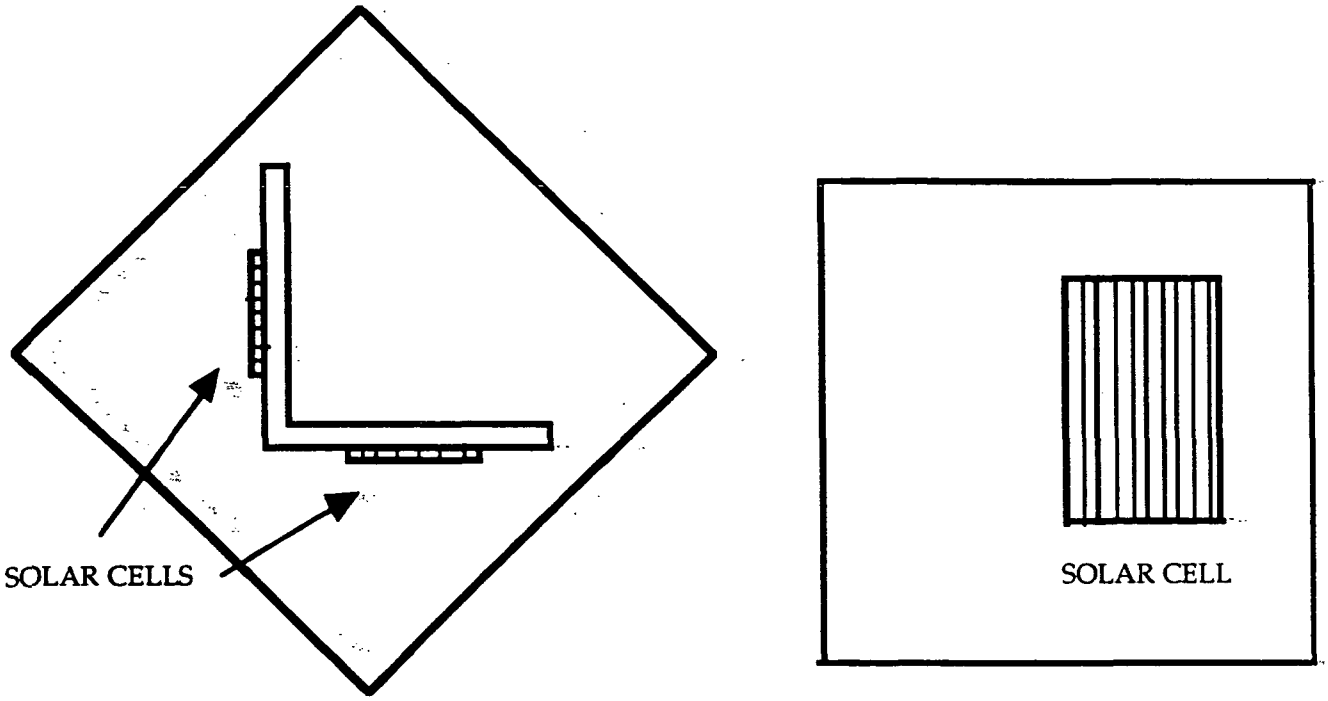

2a TOP VIEW

2b FRONT VIEW

Figure 1 SENSORS

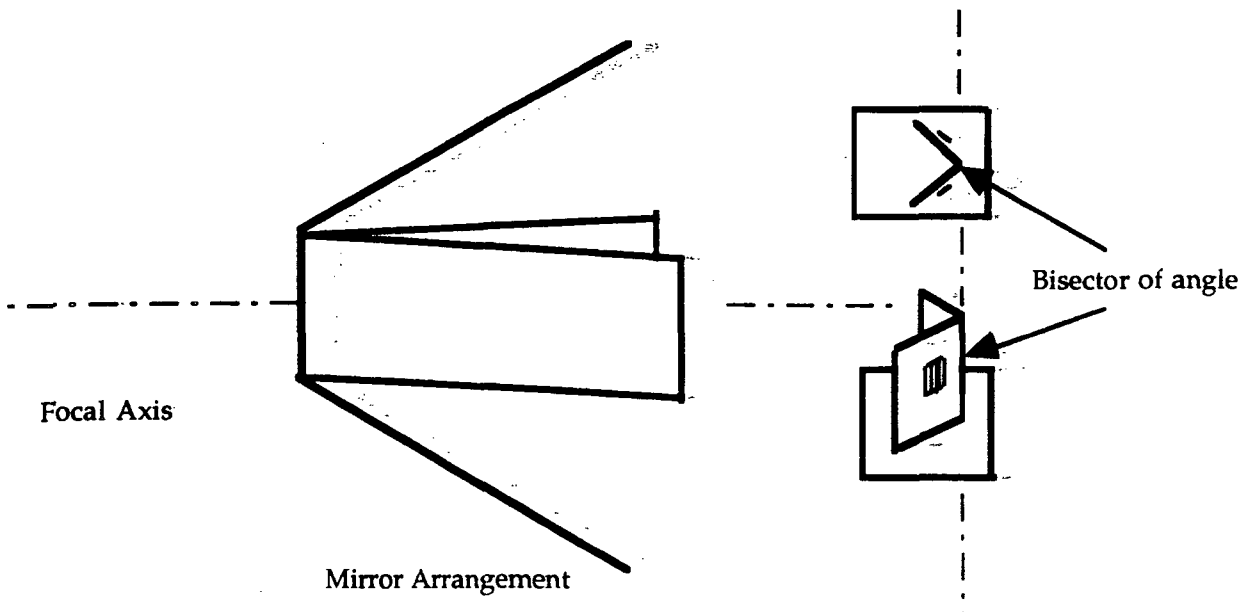

Figure 2 SOLAR TRACKER CONFIGURATION

ASPOD Control System

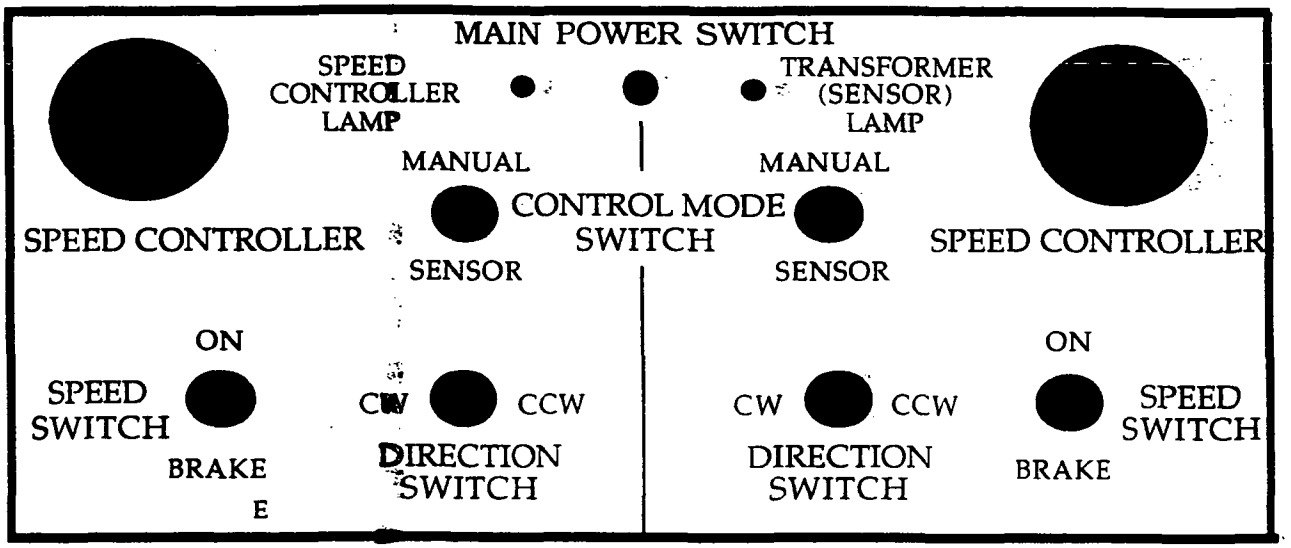

TOP VIEW

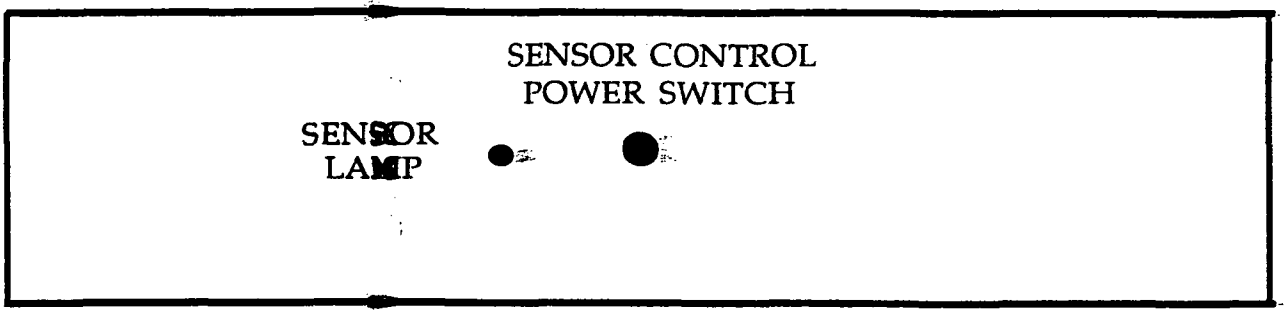

FRONT VIEW

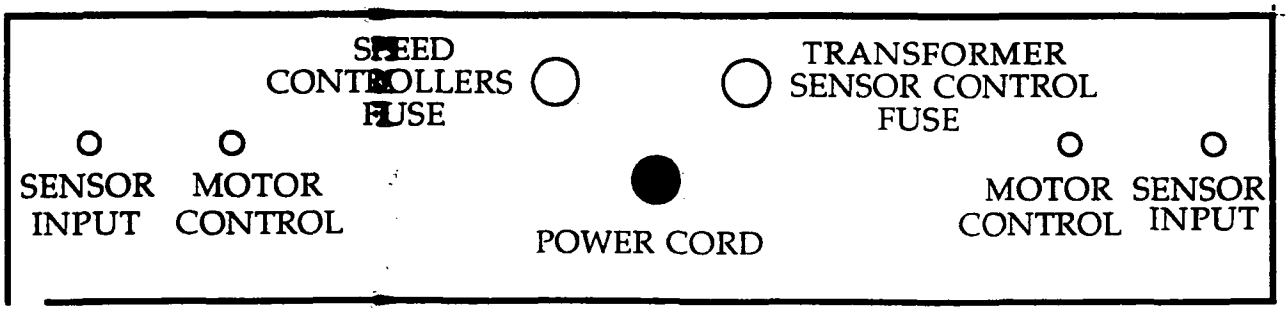

BACK VIEW

ORIGINAL PAGE IS
OF POOR QUALITY

References

1. Beard, Jonathon. Sweeping Up Space Junk, Discover, December 1988, p22.
2. Lechleitner, Hans. Raumpfleger Dringend Gesucht, March 1989, p154.
3. Beard, Jonathon. Verdens Forste Flyvende Skraldemand, Danish Science, December 1988, p46.
4. Stewart, Doug. Eyes in Orbit Keep Tabs on the World in Unexpected Ways, Smithsonian, December 1988, p70.
5. Erickson, Jim. Engineer Plans to Clean the Heavens, Arizona Daily Star, February 21, 1987.
6. Stiles, Edward. Space Junk, Tucson Citizen, February 27, 1987.
7. Hodge, Carl. 'Sweeper' Would Gather Space Debris, Arizona Republic, August 14, 1988.
8. Stiles, Edward. U of A Robot Will Collect Space Junk, Tucson Citizen, September 23, 1988.
9. Turner, Mark Holman. Trashed in Space, American Way, May 15, 1989.
10. General Accounting Office Report, April 1989.
11. Ramohalli, Kumar, et al. Autonomous Space Processor for Orbital Debris; USRA Summer Conference, June 12, 1989.
12. Johnson, Nicholas L., Darren S. McKnight. Artificial Space Debris, Orbit Book Company, Inc., Malabar, Florida, 1987.
13. Meriam,J.L., and Kraige,L.G. Engineering Mechanics Dynamics, John Wiley and Sons 1986.
14. Erdman,A.G. and Sandor,G.N., Mechanism Design:Analysis and Synthesis, Prentice Hall, 1984.
15. Shigley and Mischke Mechanical Engineering Design McGraw-Hill 1989.
16. Beer, F.P. and Johnston, E.R., Vector Mechanics for Engineers, McGraw-Hill, 1984.
17. Boylestad,Robert and Nashelsky,Louis Electronics A Survey, Prentice Hall, 1989.
18. Askeland, Donald R. The Science and Engineering of Materials, PWS Engineering, 1985.
19. Nikravesh, Parvis E. Computer Aided Analysis of Mechanical, Systems Prentice Hall, 1988.
20. Wolfson, Richard and Pasachoff, Jay M. Physics Little,Brown ,1987.
21. Kahn, M. E., and B. Roth. The Near-Minimum-Time Control of Open-Loop Articulated Kinematic Chains, J. Dyn. Syst., Meas., Contr., vol. 93, 1971.
22. Lin, C. S., P. R. Chang, and J. Y. S. Luh. Formulation and Optimization of Cubic Polynomial Trajectories for Industrial Robots, IEEE Trans. Automat. Contr., vol AC-28, 1983.
23. Bobrow, E., S. Dubowsky, and J. S. Gibson. On the Optimal Control of Robotic Manipulators with Actuator Constraints, Presented at the American Control Conf., San Fransicso, CA, 1983.
24. Bobrow, E., S. Dubowsky, and J. S. Gibson. Time-Optimal Control of Robotic Manipulators Along Specified Paths, Int. J. Robotics Res., vol 4, no. 3, (Fall) 1985.
25. Shin, K. G., N. D. McKay. An Efficient Robot Arm Control Under Geometric Path Constraints, Presented at the IEEE Conf. on Decisions and Control, San Fransisco, CA, 1983.
26. Shin, K. G., N. D. McKay. Minimum-Time Control of Robotic Manipulators with

Geometric Path Constraints, IEEE Trans. Automat. Contr., vol. AC-30 no.6, June 1985.
27. Slotine, J. S., and H. Y. Yang. Improving the Efficiency of Time-Optimal Path-Following Algorithms, IEEE Trans. Robotics and Automat., vol. 5, no. 1, 1989.
28. Singh, S., and M. C. Leu. Optimal Trajectory Generation for Robotic Manipulators Using Dynamic Programming, J. Dyn. Syst., Meas., Contr., vol. 109, 1987.
29. Jouaneh, M., D. Dornfield, and M Tomizuka. Trajectory Planning for Coordinated Motion of a Robot and a Positioning Table: Part 2 - Optimal Trajectory Specification, IEEE Trans. Automat. Contr., vol. 6, no. 6, 1990.
30. Shin, K. G., and N. D. McKay. A Dynamic Programming Approach to Trajectory Planning of Robotic Manipulators, IEEE Trans. Automat. Contr., vol. AC-31, no. 6, 1986.
31. Bellman, R., Dynamic Programming, Princeton University Press, Princeton, NJ, 1957.

APPENDIX A

DEFLECTION AND MOMENT ANALYSIS

MATERIAL ⇒ Al - 6061 - T6

MODULUS OF ELASTICITY : $E = 10.3 \times 10^6$ psi

LINK I : Square Tube

DIMENSION : 2" x 2" x 1/8" (12" length)
WEIGHT : 1.1 lb

LINK II : Square Tube

DIMENSION : 2" x 2" x 1/8" (24" length)
WEIGHT : 2.2 lb

LINK III Square Tube

DIMENSION : 2" x 2" x 1/8" (12" length)
WEIGHT : 1.1 lb

EQUATIONS

$$I = \frac{a^4}{12} - \frac{(a-2t)^4}{12} \qquad (1)$$

$$\delta = \frac{PL^3}{3EI} + \frac{ML^2}{2EI} + \frac{WL^4}{8EI} \qquad (2)$$

$$M = PL + \frac{WL^2}{2}$$

where :

I = moment of inertia
a = width of square tube
t = wall thickness
P = load at end of link
L = length of link
M = moment at end of link
E = modulus of elasticity
W = weight density
δ = deflection at end of link

DEFLECTION ANALYSIS

LINK III

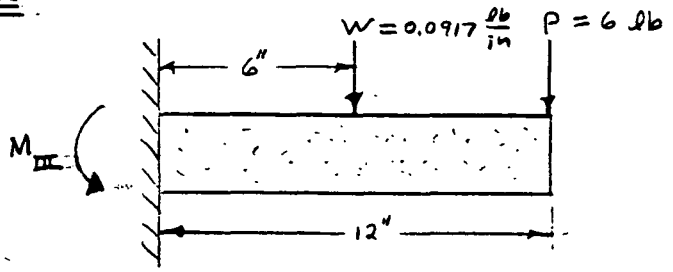

LOAD = 1 oz (0.0625 lb)

MAX. DEFLECTION = 0.39 in

$$\delta = \frac{PL^3}{3EI} + \frac{WL^4}{8EI} \qquad (\delta_{MAX})$$

$$I = \frac{(2in)^4}{12} - \frac{[(2in) - 2(1/8in)]^4}{12}$$

$$I = 0.5518\ in^4$$

	δ (unloaded)	δ (loaded)	Δ
DEFLECTION:	0.0006 in	0.0007 in	0.0001 in

$$M = PL + \frac{WL^2}{2} \qquad (M_{MAX})$$

	unloaded	loaded	Δ
TORQUE:	78.60 lb·in	79.35 lb·in	0.75 lb·in

LINK II

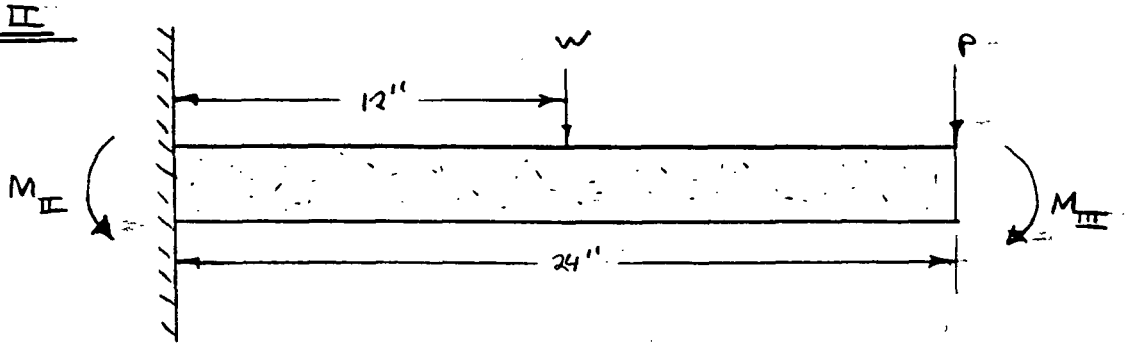

unloaded: $P = 3.7\ lb + 6\ lb + 1.1\ lb = 10.8\ lb$

loaded: $P = 10.8625\ lb$

$$\delta = \frac{PL^3}{3EI} + \frac{WL^4}{8EI} + \frac{M_{III} L^2}{2EI}$$

	unloaded	loaded	Δ
DEFLECTION:	0.0134 in	0.0135 in	0.0001 in

$$M = PL + \frac{WL^2}{2}$$

	unloaded	loaded	Δ
TORQUE:	285.61 lb·in	287.11 lb·in	1.5 lb·in

LINK III

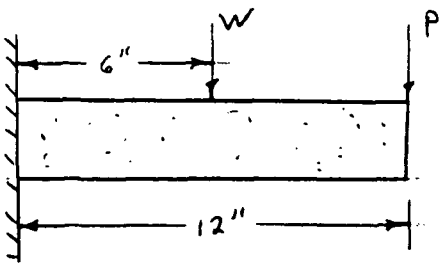

$$\delta = \frac{PL^3}{3EI} + \frac{WL^4}{8EI} + \frac{M_{II} L^2}{2EI}$$

$P_{unloaded} = 6 + 1.1 + 3.7 + 2.2 + 3.7 = 16.7$ lb

$P_{loaded} = 16.7625$ lb

	unloaded	loaded	Δ
DEFLECTION:	0.0054 in	0.0054	< 0.0001 in

$$M = PL + \frac{WL^2}{2}$$

	unloaded	loaded	Δ
MOMENT:	207.00 ft·lb		

APPENDIX B

ACCELERATION ANALYSIS

ACCELERATION DEVELOPMENT

Lagrange Equation:

$$\tau = (m l_c^2 + I)\ddot{\theta} + mg l_c \cos\theta \qquad \text{EQ.16}$$

$$\tau = [24.56\,kg\,(1.3167m)^2 + 62.12\,kg\cdot m^2]\ddot{\theta} + 24.56\,kg\,(9.81\,m/s^2)(1.3167m)\cos\theta$$

$$\tau = (104.70\,kg\cdot m^2)\ddot{\theta} + (317.2\,N\cdot m)\cos\theta$$

$$\alpha = \frac{2\theta}{t^2} \qquad \text{EQ.17}$$

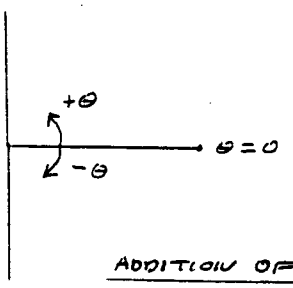

TABLE 2

FOR STATIC LOAD ONLY:

ADDITION OF CONSTANT ACCELERATION

θ (DEG)	τ (N·m)	* TIME → 60 ACC → 0.001745	44 0.003245	28 0.008014	12 0.043633
-90	0	0.18	0.34	0.84	4.57
-80	55.08	55.26	55.42	55.92	59.65
-70	108.49	108.67	108.83	109.33	113.06
-60	158.60	158.78	158.94		163.17
-50	203.89	204.07	204.23		208.46
-40	242.99	243.17	243.33		247.56
-30	274.70	274.89	275.04		279.27
-20	298.07	298.25	298.41		302.64
-10	312.38	312.56	312.72		316.95
0	317.20	317.38	317.54		321.77
10	312.38	312.20			316.95
20	298.07	297.89			302.64
30	274.70	274.52			279.27
40	242.99	242.81			247.56
50	203.89	203.71			208.46
60	158.60	158.42			163.17
70	108.49	108.31			113.06
80	55.08	54.90			59.65
90	0	-0.18			4.57

* Time is time required to move manipulator from the fully down position (6'oclock) to the fully up position (12'oclock) using constant acceleration until the horizontal position is reached and then the negative of that acceleration to the 12'oclock position.